

# Interrogating theoretical models of neural computation with deep inference

Sean R. Bittner, Agostina Palmigiano, Alex T. Piet, Chunyu A. Duan, Carlos D. Brody,  
Kenneth D. Miller, and John P. Cunningham.

## <sup>1</sup> 1 Abstract

<sup>2</sup> The cornerstone of theoretical neuroscience is the circuit model: a system of equations that captures  
<sup>3</sup> a hypothesized neural mechanism of scientific importance. Such models are valuable when they give  
<sup>4</sup> rise to an experimentally observed phenomenon – whether behavioral or in terms of neural activity –  
<sup>5</sup> and thus can offer insight into neural computation. The operation of these circuits, like all models,  
<sup>6</sup> critically depends on the choices of model parameters. Historically, the gold standard has been  
<sup>7</sup> to analytically derive the relationship between model parameters and computational properties.  
<sup>8</sup> However, this enterprise quickly becomes infeasible as biologically realistic constraints are included  
<sup>9</sup> into the model increasing its complexity, often resulting in *ad hoc* approaches to understanding  
<sup>10</sup> the relationship between model and computation. We bring recent machine learning techniques –  
<sup>11</sup> the use of deep generative models for probabilistic inference – to bear on this problem, learning  
<sup>12</sup> distributions of parameters that produce the specified properties of computation. Importantly, the  
<sup>13</sup> techniques we introduce offer a principled means to understand the implications of model parameter  
<sup>14</sup> choices on computational properties of interest. We motivate this methodology with a worked  
<sup>15</sup> example analyzing sensitivity in the stomatogastric ganglion. We then use it to generate insights  
<sup>16</sup> into neuron-type input-responsivity in a model of primary visual cortex, a new understanding  
<sup>17</sup> of rapid task switching in superior colliculus models, and attribution of bias in recurrent neural  
<sup>18</sup> networks solving a toy mathematical problem. More generally, this work offers a quantitative  
<sup>19</sup> grounding for theoretical models going forward, pointing a way to how rigorous statistical inference  
<sup>20</sup> can enhance theoretical neuroscience at large.

## <sup>21</sup> 2 Introduction

<sup>22</sup> The fundamental practice of theoretical neuroscience is to use a mathematical model to understand  
<sup>23</sup> neural computation, whether that computation enables perception, action, or some intermediate  
<sup>24</sup> processing [1]. In this field, a neural computation is systematized with a set of equations – the  
<sup>25</sup> model – and these equations are motivated by biophysics, neurophysiology, and other conceptual  
<sup>26</sup> considerations. The function of this system is governed by the choice of model parameters, which

27 when configured appropriately, give rise to a measurable signature of a computation. The work of  
28 analyzing a model then becomes the inverse problem: given a computation of interest, how can we  
29 reason about these suitable parameter configurations – their likely values, their uniquenesses and  
30 degeneracies, their attractor states and phase transitions, and more?

31 Consider the idealized practice: a theorist considers a model carefully and analytically derives how  
32 model parameters govern the computation. Seminal examples of this gold standard include our  
33 field’s understanding of memory capacity in associative neural networks [2], chaos and autocorrela-  
34 tion timescales in random neural networks [3], and the paradoxical effect in excitatory/inhibitory  
35 networks [4]. Unfortunately, as circuit models include more biological realism, theory via analytic  
36 derivation becomes intractable. This fact creates an unfavorable tradeoff for the theorist. On the  
37 one hand, one may tractably analyze systems of equations with unrealistic assumptions (for ex-  
38 ample symmetry or gaussianity), producing accurate inferences about parameters of a too-simple  
39 model. On the other hand, one may choose a more biologically relevant model at the cost of *ad hoc*  
40 approaches to analysis (simply examining simulated activity), producing questionable or partial  
41 inferences about parameters of an appropriately complex, scientifically relevant model.

42 Of course, this same tradeoff has been confronted in many scientific fields and engineering problems  
43 characterized by the need to do inference in complex models. In response, the machine learning  
44 community has made remarkable progress in recent years, via the use of deep neural networks as a  
45 powerful inference engine: a flexible function family that can map observed phenomena (in this case  
46 the measurable signal of some computation) back to probability distributions quantifying the likely  
47 parameter configurations. One celebrated example of this approach from the machine learning  
48 community, from which we draw key inspiration for this work, is the variational autoencoder [5, 6],  
49 which uses a deep neural network to induce an (approximate) posterior distribution on hidden  
50 variables in a latent variable model, given data. Indeed, these tools have been used to great success  
51 in neuroscience as well, in particular for interrogating parameters (sometimes treated as hidden  
52 states) in models of both cortical population activity [7, 8, 9, 10] and animal behavior [11, 12, 13].  
53 These works have used deep neural networks to expand the expressivity and accuracy of statistical  
54 models of neural data [14].

55 However, these inference tools have not significantly influenced the study of theoretical neuroscience  
56 models, for at least three reasons. First, at a practical level, the nonlinearities and dynamics of  
57 many theoretical models are such that conventional inference tools typically produce a narrow  
58 set of insights into these models. Indeed, only in the last few years has deep learning research

59 advanced to a point of relevance to this class of problem. Second, the object of interest from a  
60 theoretical model is not typically data itself, but rather a qualitative phenomenon – inspection of  
61 model behavior, or better, a measurable signature of some computation – an *emergent property* of  
62 the model. Third, because theoreticians work carefully to construct a model that has biological  
63 relevance, such a model as a result often does not fit cleanly into the framing of a statistical model.  
64 Technically, because many such models stipulate a noisy system of differential equations that can  
65 only be sampled or realized through forward simulation, they lack the explicit likelihood and priors  
66 central to the probabilistic modeling toolkit.

67 To address these three challenges, we developed an inference methodology – ‘emergent property  
68 inference’ – which learns a distribution over parameter configurations in a theoretical model. Crit-  
69 ically, this distribution is such that draws from the distribution (parameter configurations) corre-  
70 spond to systems of equations that give rise to a specified emergent property. First, we stipulate a  
71 bijective deep neural network that induces a flexible family of probability distributions over model  
72 parameterizations with a probability density we can calculate [15, 16, 17]. Second, we quantify  
73 the notion of emergent properties as a set of moment constraints on datasets generated by the  
74 model. Thus, an emergent property is not a single data realization, but a phenomenon or a feature  
75 of the model, which is ultimately the object of interest to the theorist (compared to the statisti-  
76 cal neuroscientist). Conditioning on an emergent property requires a variant of deep probabilistic  
77 inference methods, which we have previously introduced [18]. Third, because we cannot assume  
78 the theoretical model has explicit likelihood on data or the emergent property of interest, we use  
79 stochastic gradient techniques in the spirit of likelihood free variational inference [19]. Taken to-  
80 gether, emergent property inference (EPI) provides a methodology for inferring and then reasoning  
81 about parameter configurations that give rise to particular emergent phenomena in theoretical  
82 models. To clarify the technical details of EPI, we use it to analyze network syncing in a classic  
83 model of the stomatogastric ganglion [20].

84 Equipped with this methodology, we then investigated three models of current importance in theo-  
85 retical neuroscience. These models were chosen to demonstrate generality through ranges of biolog-  
86 ical realism (conductance-based biophysics to recurrent neural networks), neural system function  
87 (pattern generation to abstract cognitive function), and network scale (four to infinite neurons).  
88 First, we use EPI to produce a set of verifiable hypotheses of input-responsivity in a four neuron-  
89 type dynamical model of primary visual cortex; we then validate these hypotheses in the model.  
90 Second, we demonstrated how the systematic application of EPI to levels of task performance can

91 generate experimentally testable hypotheses regarding connectivity in superior colliculus. Third,  
 92 we use EPI to uncover the sources of bias in a low-rank recurrent neural network executing a toy  
 93 mathematical computation. The novel scientific insights offered by EPI contextualize and clarify  
 94 the previous studies exploring these models [20, 21, 22, 23] and more generally, suggests a depar-  
 95 ture from realism vs tractability considerations towards the use of modern machine learning for  
 96 sophisticated interrogation of biologically relevant models.

97 We note that, during our preparation and early presentation of this work [24, 25], another work  
 98 has arisen with broadly similar goals: bringing statistical inference to mechanistic models of neural  
 99 circuits [26]. We are excited by this broad problem being recognized by the community, and we  
 100 emphasize that these works offer complementary neuroscientific contributions and use different  
 101 technical methodologies. Scientifically, our work has focused primarily on systems-level theoretical  
 102 models, while their focus has been on lower-level cellular models. Secondly, there are several key  
 103 technical differences in the approaches (see Section A.1.4) perhaps most notably is our focus on  
 104 the emergent property – the measurable signal of the computation in question, vs their focus  
 105 on observed datasets; both certainly are worthy pursuits. The existence of these complementary  
 106 methodologies emphasizes the increased importance and timeliness of both works.

## 107 3 Results

### 108 3.1 Motivating emergent property inference of theoretical models

109 Consideration of the typical workflow of theoretical modeling clarifies the need for emergent prop-  
 110 erty inference. First, the theorist designs or chooses an existing model that, it is hypothesized,  
 111 captures the computation of interest. To ground this process in a well-known example, consider  
 112 the stomatogastric ganglion (STG) of crustaceans, a small neural circuit which generates multiple  
 113 rhythmic muscle activation patterns for digestion [27]. Despite full knowledge of STG connectivity  
 114 and a precise characterization of its rhythmic pattern generation, biophysical models of the STG  
 115 have complicated relationships between circuit parameters and neural activity [28]. A model of the  
 116 STG [20] is shown schematically in Figure 1A, and note that the behavior of this model will be crit-  
 117 ically dependent on its parameterization – the choices of conductance parameters  $z = [g_{el}, g_{synA}]$ .  
 118 Specifically, the two fast neurons ( $f_1$  and  $f_2$ ) mutually inhibit one another, and oscillate at a  
 119 faster frequency than the mutually inhibiting slow neurons ( $s_1$  and  $s_2$ ), and the hub neuron (hub)  
 120 couples with the fast or slow population or both.

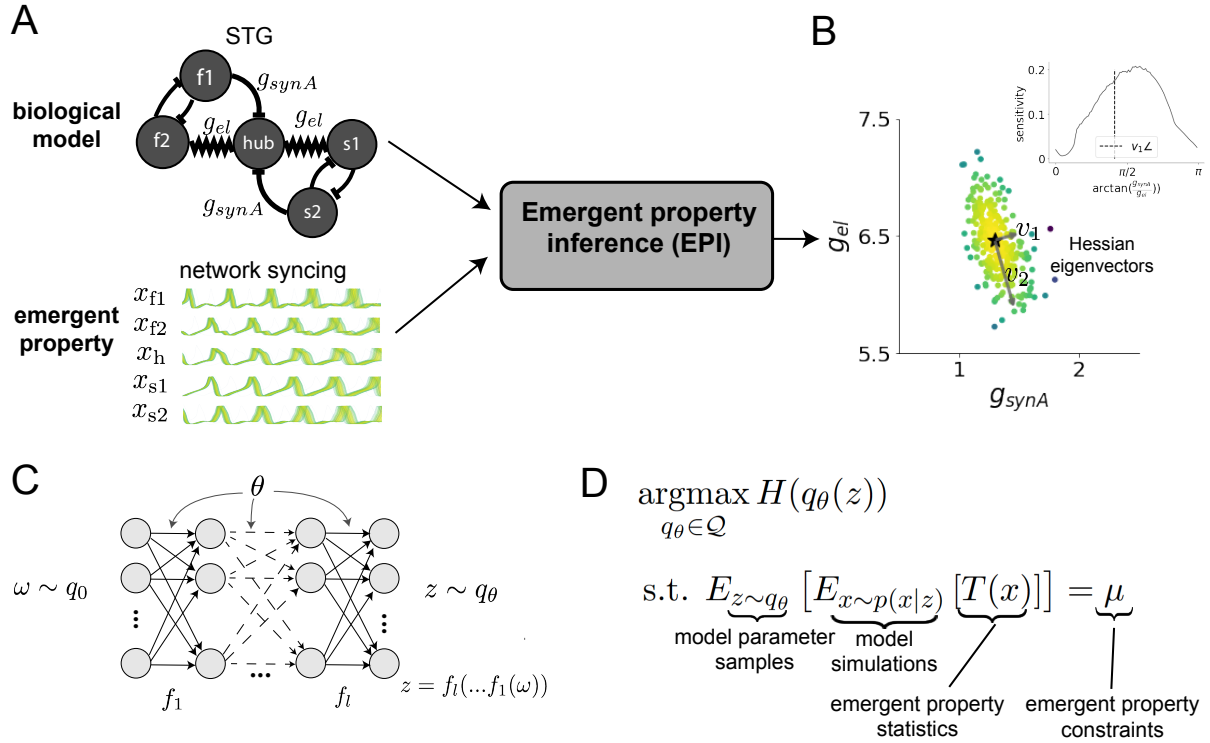


Figure 1: Emergent property inference (EPI) in the stomatogastric ganglion. A. For a choice of model (STG) and emergent property (network syncing), emergent property inference (EPI) learns a posterior distribution of the model parameters  $z = [g_{\text{el}}, g_{\text{synA}}]^T$  conditioned on network syncing. B. An EPI distribution of STG model parameters producing network syncing. The eigenvectors of the Hessian at the mode of the inferred distribution are indicated as  $v_1$  and  $v_2$ . (Inset) Sensitivity of the system with respect to network syncing along all dimensions of parameter space away from the mode. (see Section A.2.1). C. Deep probability distributions map a latent random variable  $\omega \sim q_0$ , where  $q_0$  is chosen to be simple distribution such as an isotropic gaussian, through a highly expressive function family  $f_\theta(\omega) = f_l(\dots f_1(\omega))$  parameterized by the neural network weights and biases  $\theta \in \Theta$ . This mapping induces an implicit probability model  $q(g_\theta(\omega)) \in \mathcal{Q}$  D. EPI learns a distribution  $q_\theta(z)$  of model parameters that produce an emergent property: the emergent property statistics  $T(x)$  are fixed in expectation over parameter distribution samples  $z \sim q_\theta(z)$  to particular values  $\mu$ . EPI distributions maximize randomness via entropy, although other measures are sensible.

121 Second, once the model is selected, the theorist defines the emergent property, the measurable  
 122 signal of scientific interest. To continue our running STG example, one such emergent property  
 123 is the phenomenon of *network syncing* – in certain parameter regimes, the frequency of the hub  
 124 neuron matches that of the fast and slow populations at an intermediate frequency. This emergent  
 125 property is shown in Figure 1A at a frequency of 0.55Hz.

126 Third, qualitative parameter analysis ensues: since precise mathematical analysis is intractable in  
 127 this model, a brute force sweep of parameters is done [20]. Subsequently, a qualitative description is  
 128 formulated to describe of the different parameter configurations that lead to the emergent property.  
 129 In this last step lies the opportunity for a precise quantification of the emergent property as a  
 130 statistical feature of the model. Once we have such a methodology, we can infer a probability  
 131 distribution over parameter configurations that produce this emergent property.

132 Before presenting technical details (in the following section), let us understand emergent property  
 133 inference schematically: the black box in Figure 1A takes, as input, the model and the specified  
 134 emergent property, and produces as output the parameter distribution shown in Figure 1B. This  
 135 distribution – represented for clarity as samples from the distribution – is then a scientifically  
 136 meaningful and mathematically tractable object. It conveys parameter regions critical to the emer-  
 137 gent property, directions in parameter space that will be invariant (or not) to that property, and  
 138 more. In the STG model, this distribution can be specifically queried to determine the prototypical  
 139 parameter configuration for network syncing (the mode; Figure 1B star), and then how quickly  
 140 network syncing will decay based on changes away from that mode. The inset of Figure 1B vali-  
 141 dates that indeed network syncing behaves as the distribution predicts, when moving away from  
 142 the mode (Figure 1B star). Further validation of EPI is available in the supplementary materials,  
 143 where we analyze a simpler model for which ground-truth statements can be made (Section A.1.1).

### 144 3.2 A deep generative modeling approach to emergent property inference

145 Emergent property inference (EPI) systematizes the three-step procedure of the previous section.  
 146 First, we consider the model as a coupled set of differential (and potentially stochastic) equations  
 147 [20]. In the running STG example, the dynamical state  $x = [x_{f1}, x_{f2}, x_{hub}, x_{s1}, x_{s2}]$  is the membrane  
 148 potential for each neuron, which evolves according to the biophysical conductance-based equation:

$$C_m \frac{dx}{dt} = -h(x; z) = -[h_{leak}(x; z) + h_{Ca}(x; z) + h_K(x; z) + h_{hyp}(x; z) + h_{elec}(x; z) + h_{syn}(x; z)] \quad (1)$$

where  $C_m = 1\text{nF}$ , and  $h_{\text{leak}}$ ,  $h_{Ca}$ ,  $h_K$ ,  $h_{\text{hyp}}$ ,  $h_{\text{elec}}$ ,  $h_{\text{syn}}$  are the leak, calcium, potassium, hyperpolarization, electrical, and synaptic currents, all of which have their own complicated dependence on  $x$  and  $z = [g_{\text{el}}, g_{\text{synA}}]$  (see Section A.2.1).

Second, we define the emergent property, which as above is network syncing: oscillation of the entire population at an intermediate frequency of our choosing (Figure 1A bottom). Quantifying this phenomenon is straightforward: we define network syncing to be that each neuron’s spiking frequency – denoted  $\omega_{\text{f1}}(x)$ ,  $\omega_{\text{f2}}(x)$ , etc. – is close to an intermediate frequency of 0.55Hz. Mathematically, we achieve this via constraints on the mean and variance of  $\omega_i(x)$  for each neuron  $i \in \{\text{f1}, \text{f2}, \text{hub}, \text{s1}, \text{s2}\}$ , and thus:

$$E[T(x)] \triangleq E \begin{bmatrix} \omega_{\text{f1}}(x) \\ \vdots \\ (\omega_{\text{f1}}(x) - 0.55)^2 \\ \vdots \end{bmatrix} = \begin{bmatrix} 0.55 \\ \vdots \\ 0.025^2 \\ \vdots \end{bmatrix} \triangleq \mu, \quad (2)$$

which completes the quantification of the emergent property.

Third, we perform emergent property inference: we find a distribution over parameter configurations  $z$ , and insist that samples from this distribution produce the emergent property; in other words, they obey the constraints introduced in Equation 2. This distribution will be chosen from a family of probability distributions  $\mathcal{Q} = \{q_\theta(z) : \theta \in \Theta\}$ , defined by a deep generative distribution of the normalizing flow class [15, 16, 17] – neural networks which transform a simple distribution into a suitably complicated distribution (as is needed here). This deep distribution is represented in Figure 1C (and see Methods for more detail). Then, mathematically, we must solve the following optimization program:

$$\begin{aligned} & \underset{q_\theta \in \mathcal{Q}}{\operatorname{argmax}} H(q_\theta(z)) \\ & \text{s.t. } E_{z \sim q_\theta} [E_{x \sim p(x|z)} [T(x)]] = \mu, \end{aligned} \quad (3)$$

where  $T(x), \mu$  are defined as in Equation 2, and  $p(x|z)$  is the intractable distribution of data from the model ( $x$ ), given that model’s parameters  $z$  (we access samples from this distribution by running the model forward). The purpose of each element in this program is detailed in Figure 1D. Finally, we recognize that many distributions in  $\mathcal{Q}$  will respect the emergent property constraints, so we require a normative principle to select amongst them. This principle is captured in Equation 3 by the primal objective  $H$ . Here we chose Shannon entropy as a means to find parameter distributions with minimal assumptions beyond some chosen structure [29, 30, 18, 31], but we emphasize that

<sup>174</sup> the EPI method is unaffected by this choice (but the results of course will depend on the primal  
<sup>175</sup> objective chosen).

<sup>176</sup> EPI optimizes the weights and biases  $\theta$  of the deep neural network (which induces the probability  
<sup>177</sup> distribution) by iteratively solving Equation 3. The optimization is complete when the sampled  
<sup>178</sup> models with parameters  $z \sim q_\theta$  produce activity consistent with the specified emergent property.  
<sup>179</sup> Such convergence is evaluated with a hypothesis test that the mean of each emergent property  
<sup>180</sup> statistic is not different than its emergent property value (see Section A.1.2). Equipped with this  
<sup>181</sup> method, we now prove out the value of EPI by using it to investigate three prominent models in  
<sup>182</sup> neuroscience, using EPI to produce new insights about these models.

<sup>183</sup> **3.3 Comprehensive input-responsivity in a nonlinear sensory system**

<sup>184</sup> In studies of primary visual cortex (V1), theoretical models with excitatory (E) and inhibitory  
<sup>185</sup> (I) populations have reproduced a host of experimentally documented phenomena. In particular  
<sup>186</sup> regimes of excitation and inhibition, these E/I models exhibit the paradoxical effect [4], selective  
<sup>187</sup> amplification [32], surround suppression [33], and sensory integrative properties [34]. Extending  
<sup>188</sup> this model using experimental evidence of three genetically-defined classes of inhibitory neurons  
<sup>189</sup> [35, 36], recent work [21] has investigated a four-population model – excitatory (E), parvalbumin  
<sup>190</sup> (P), somatostatin (S), and vasointestinal peptide (V) neurons – as shown in Fig. 2A. The dynamical  
<sup>191</sup> state of this model is the firing rate of each neuron-type population  $x = [x_E, x_P, x_S, x_V]^\top$ , which  
<sup>192</sup> evolves according to rectified ( $\llbracket \cdot \rrbracket_+$ ) and exponentiated dynamics:

$$\tau \frac{dx}{dt} = -x + [Wx + h]_+^n \quad (4)$$

<sup>193</sup> with effective connectivity weights  $W$  and input  $h$ . In our analysis, we set the time constant  
<sup>194</sup>  $\tau = 20\text{ms}$  and dynamics coefficient  $n = 2$ . Also, as is fairly standard, we obtain an informative  
<sup>195</sup> estimate of the effective connectivities between these neuron-types  $W$  in mice by multiplying their  
<sup>196</sup> probability of connection with their average synaptic strength [37, 38] (see Section A.2.2). Given  
<sup>197</sup> these fixed choices of  $W$ ,  $n$ , and  $\tau$ , we studied the system’s response to input

$$h = b + dh, \quad (5)$$

<sup>198</sup> where the input  $h$  is comprised of a baseline input  $b = [b_E, b_P, b_S, b_V]^\top$  and a differential input  
<sup>199</sup>  $dh = [dh_E, dh_P, dh_S, dh_V]^\top$  to each neuron-type population. Throughout subsequent analyses, the  
<sup>200</sup> baseline input is  $b = [1, 1, 1, 1]^\top$ .

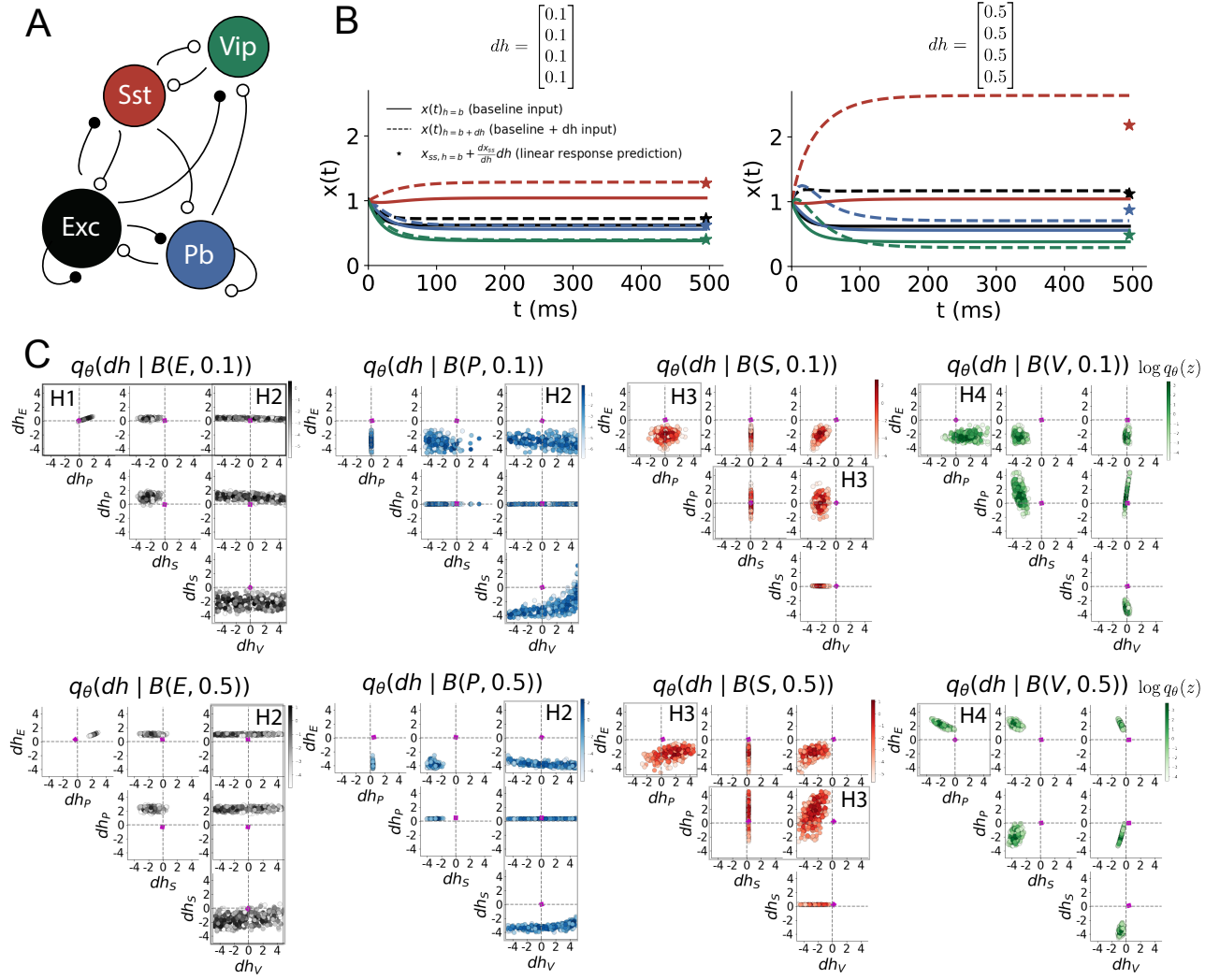


Figure 2: Hypothesis generation through EPI in a V1 model. A. Four-population model of primary visual cortex with excitatory (black), parvalbumin (blue), somatostatin (red), and vip (green) neurons. Some neuron-types largely do not form synaptic projections to others (excitatory and inhibitory projections filled and unfilled, respectively). B. Linear response predictions become inaccurate with greater input strength. V1 model simulations for input ( $b$ ) solid and ( $b + dh$ ) dashed.  $b = [1, 1, 1, 1]^T$  and (left)  $dh = [0.1, 0.1, 0.1, 0.1]^T$  (right)  $dh = [0.5, 0.5, 0.5, 0.5]^T$ . Stars indicate the linear response prediction. C. EPI distributions on differential input  $dh$  conditioned on differential response  $B(\alpha, y)$ . Supporting evidence for the four generated hypotheses are indicated by gray boxes with labels H1, H2, H3, and H4. The linear prediction from two standard deviations away from  $y$  (from negative to positive) is overlaid in magenta (very small, near origin).

Having established our model, we now define the emergent property. We begin with the linearized response of the system to input  $\frac{dx_{ss}}{dh}$  at the steady state  $x_{ss}$ , i.e. a fixed point. While this linearization accurately predicts differential responses  $dx_{ss} = [dx_{E,ss}, dx_{P,ss}, dx_{S,ss}, dx_{V,ss}]$  for small differential inputs to each population  $dh = [0.1, 0.1, 0.1, 0.1]$  (Fig. 2B, left), linearization is a poor predictor in this nonlinear model more generally (Fig. 3B, right). Currently available approaches to deriving the steady state response of this system are limited.

To get a more comprehensive picture of the input-responsivity of each neuron-type, we used EPI to learn a distribution of the differential inputs to each population  $dh$  that produce an increase of  $y \in \{0.1, 0.5\}$  in the rate of each neuron-type population  $\alpha \in \{E, P, S, V\}$ . We want to know the differential inputs  $dh$  that result in a differential steady state  $dx_{\alpha,ss}$  (the change in  $x_{\alpha,ss}$  when receiving input  $h = b + dh$  with respect to the baseline  $h = b$ ) of value  $y$  with some small, arbitrarily chosen amount of variance  $0.01^2$ . These statements amount to the emergent property

$$\mathcal{B}(\alpha, y) \triangleq E \begin{bmatrix} dx_{\alpha,ss} \\ (dx_{\alpha,ss} - y)^2 \end{bmatrix} = \begin{bmatrix} y \\ 0.01^2 \end{bmatrix} \quad (6)$$

We continue to use  $\mathcal{B}(\cdot)$  throughout the rest of the study as short hand for emergent property, which represents a different signature of computation in each application. In Each column of Figure 2C visualizes the inferred distribution of  $dh$  corresponding to a excitatory (red), parvalbumin (blue), somatostatin (red) and vip (green) neuron-type increase, while each row corresponds to amounts of increase 0.1 and 0.5. These distributions conditioned on such emergent properties are now available through EPI. For each pair of parameters we show the two-dimensional marginal distribution of samples colored by  $\log q_\theta(dh \mid \mathcal{B}(\alpha, y))$ . The inferred distributions immediately suggest four hypotheses:

221

- 222 H1: as is intuitive, each neuron-type's firing rate should be sensitive to that neuron-type's direct input (e.g. Fig. 2C H1 indicates low variance in  $dh_E$  when  $\alpha = E$ . Same observation in all inferred distributions);
- 225 H2: the E- and P-populations should be largely unaffected by  $dh_V$  (Fig. 2C H2 indicates high variance in  $dh_V$  when  $\alpha \in \{E, P\}$ );
- 227 H3: the S-population should be largely unaffected by  $dh_P$  (Fig. 2C H3 indicate high variance in  $dh_P$  when  $\alpha = S$ );
- 229 H4: there should be a nonmonotonic response of  $dx_{V,ss}$  with  $dh_E$  (Fig. 2C H4 indicates that negative  $dh_E$  should result in small  $dx_{V,ss}$ , but positive  $dh_E$  should elicit a larger  $dx_{V,ss}$ );

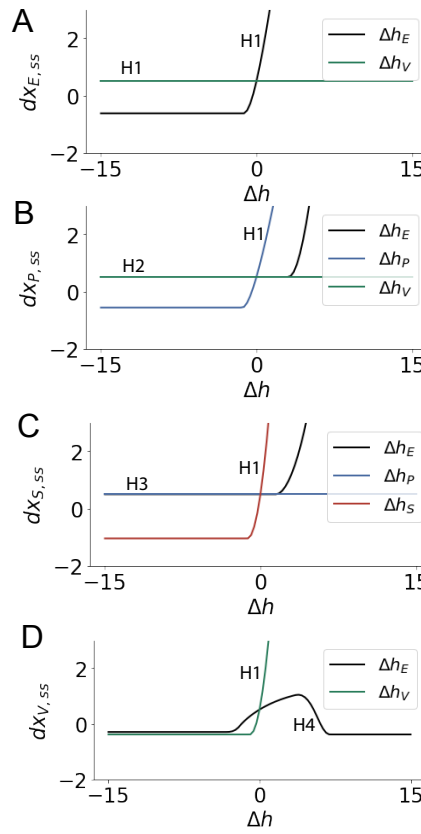


Figure 3: Confirming EPI generated hypotheses in V1. A. Differential responses by the E-population to changes in individual input  $\Delta h_\alpha u_\alpha$  away from the mode of the EPI distribution  $dh^*$ . B-D Same plots for the P-, S-, and V-populations. Labels H1, H2, H3, and H4 indicate which curves confirm which hypotheses.

231 We evaluate these hypotheses by taking steps in individual neuron-type input  $\Delta h_\alpha$  away from the  
232 modes of the inferred distributions at  $y = 0.1$ .

$$dh^* = z^* = \operatorname{argmax}_z \log q_\theta(z | \mathcal{B}(\alpha, 0.1)) \quad (7)$$

233 Now,  $dx_{\alpha,ss}$  is the steady state response to the system with input  $h = b + dh^* + \Delta h_\alpha u_\alpha$  where  $u_\alpha$   
234 is a unit vector in the dimension of  $\alpha$ . The EPI-generated hypotheses are confirmed.

- 235 • the neuron-type responses are sensitive to their direct inputs (Fig. 3A black, 3B blue, 3C  
236 red, 3D green);
- 237 • the E- and P-populations are not affected by  $dh_V$  (Fig. 3A green, 3B green);
- 238 • the S-population is not affected by  $dh_P$  (Fig. 3C blue);
- 239 • the V-population exhibits a nonmonotonic response to  $dh_E$  (Fig. 3D black), and is in fact  
240 the only population to do so (Fig. 3A-C black).

241 These hypotheses were in stark contrast to what was available to us via traditional analytical linear  
242 prediction (Fig. 2C, magenta). To this point, we have shown the utility of EPI on relatively low-  
243 level emergent properties like network syncing and differential neuron-type population responses.

<sup>244</sup> In the remainder of the study, we focus on using EPI to understand models of more abstract  
<sup>245</sup> cognitive function.

<sup>246</sup> **3.4 Identifying neural mechanisms of behavioral learning.**

<sup>247</sup> Identifying measurable biological changes that result in improved behavior is important for neuro-  
<sup>248</sup> science, since they may indicate how the learning brain adapts. In a rapid task switching experiment  
<sup>249</sup> [39], rats were explicitly cued on each trial to either orient towards a visual stimulus in the Pro  
<sup>250</sup> (P) task or orient away from a visual stimulus in the Anti (A) task (Fig. 3a). Neural recordings  
<sup>251</sup> in the midbrain supeior colliculus (SC) exhibited two population of neurons that simultaneously  
<sup>252</sup> represented both task context (Pro or Anti) and motor response (contralateral or ipsilateral to the  
<sup>253</sup> recoreded side): the Pro/Contra and Anti/Ipsi neurons [22]. Duan et al. proposed a model of SC  
<sup>254</sup> that, like the V1 model analyzed in the previous section, is a four-population dynamical system.  
<sup>255</sup> Here, the neuron-type populations are functionally-defined as the Pro- and Anti-populations in each  
<sup>256</sup> hemisphere (left (L) and right (R)). The Pro- or Anti-populations receive an input determined by  
<sup>257</sup> the cue, and then the left and right populations receive an input based on the side of the light  
<sup>258</sup> stimulus. Activities were bounded between 0 and 1, so that a high output of the Pro population  
<sup>259</sup> in a given hemisphere corresponds to the contralateral response. An additional stipulation is that  
<sup>260</sup> when one Pro population responds with a high-output, the opposite Pro population must respond  
<sup>261</sup> with a low output. Finally, this circuit operates in the presence of gaussian noise resulting in trial-  
<sup>262</sup> to-trial variability (see Section A.2.3). The connectivity matrix is parameterized by the geometry  
<sup>263</sup> of the population arrangement (Fig. 3B).

<sup>264</sup> Here, we used EPI to learn distributions of the SC weight matrix parameters  $z = W$  conditioned  
<sup>265</sup> on of various levels of rapid task switching accuracy  $\mathcal{B}(p)$  for  $p \in \{50\%, 60\%, 70\%, 80\%, 90\%\}$  (see  
<sup>266</sup> Section A.2.3). Following the approach in Duan et al., we decomposed the connectivity matrix  
<sup>267</sup>  $W = QAQ^{-1}$  in such a way (the Schur decomposition) that the basis vectors  $q_i$  are the same for all  
<sup>268</sup>  $W$  (Fig. 3C). These basis vectors have intuitive roles in processing for this task, and are accordingly  
<sup>269</sup> named the *all* mode - all neurons co-fluctuate, *side* mode - one side dominates the other, *task* mode  
<sup>270</sup> - the Pro or Anti populations dominate the other, and *diag* mode - Pro- and Anti-populations of  
<sup>271</sup> opposite hemispheres dominate the opposite pair. The corresponding eigenvalues (e.g.  $a_{\text{task}}$ , which  
<sup>272</sup> change according to  $W$ ) indicate the degree to which activity along that mode is increased or  
<sup>273</sup> decreased by  $W$ .

<sup>274</sup> EPI demonstrates that, for greater task accuracies, the task mode eigenvalue increases, indicating

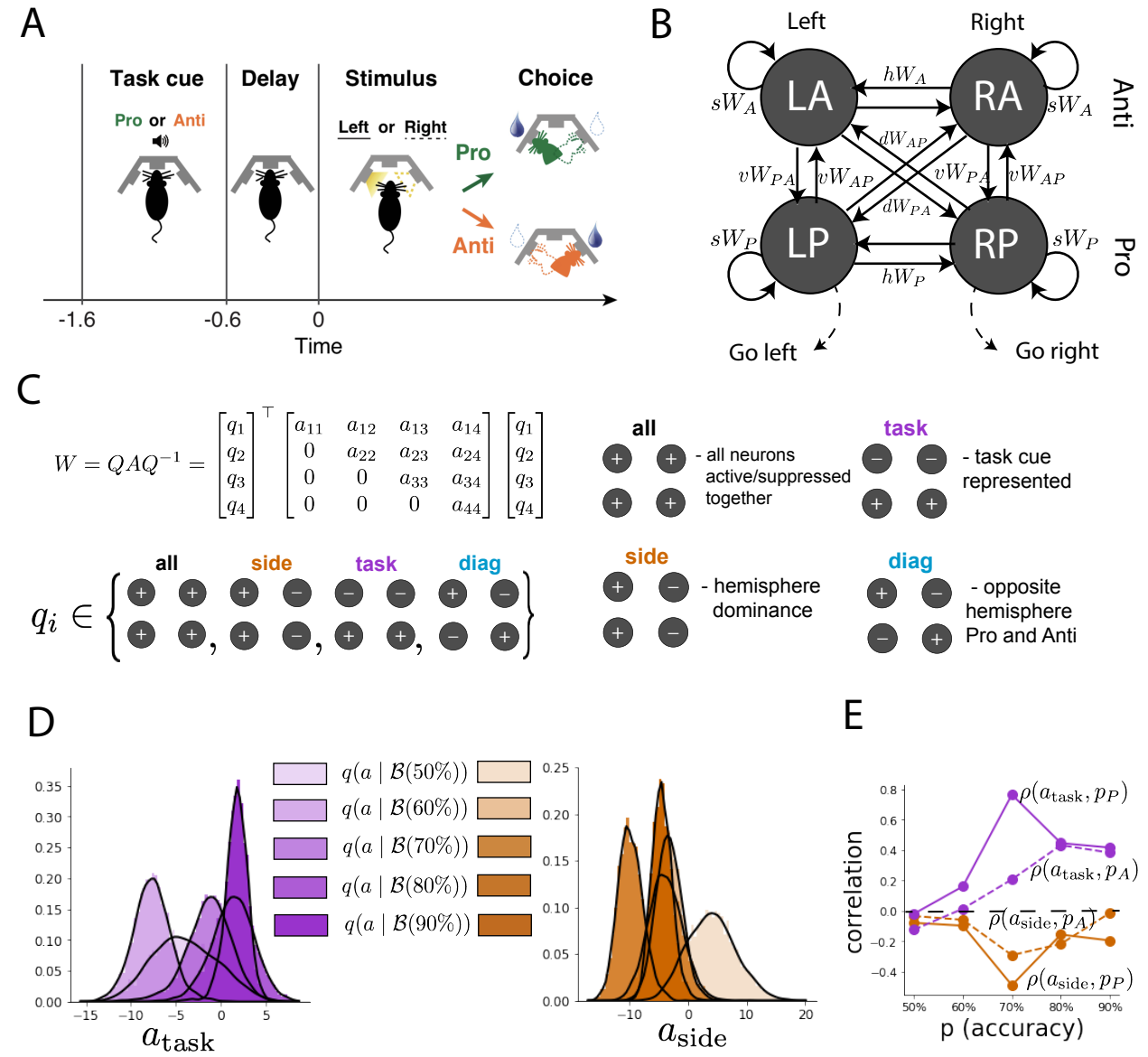


Figure 4: EPI reveals changes in SC [22] connectivity that control task accuracy. A. Rapid task switching behavioral paradigm (see text). B. Model of superior colliculus (SC). Neurons: LP - left pro, RP - right pro, LA - left anti, RA - right anti. Parameters:  $sW$  - self,  $hW$  - horizontal,  $vW$  - vertical,  $dW$  - diagonal weights. C. The Schur decomposition of the weight matrix  $W = QAQ^{-1}$  is a unique decomposition with orthogonal  $Q$  and upper triangular  $A$ . Schur modes:  $q_{\text{all}}$ ,  $q_{\text{task}}$ ,  $q_{\text{side}}$ , and  $q_{\text{diag}}$ . D. The marginal EPI distributions of the Schur eigenvalues at each level of task accuracy. E. The correlation of Schur eigenvalue with task performance in each learned EPI distribution.

the importance of  $W$  to the task representation (Fig. 4D, purple). Stepping from random chance (50%) networks to marginally task-performing (60%) networks, there is a marked decrease of the side mode eigenvalues (Fig. 3D, orange). Such side mode suppression remains in the models achieving greater accuracy, revealing its importance towards task performance. There were no interesting trends with learning in the all or diag mode (hence not shown in Fig. 3). Importantly, we can conclude from our methodology that side mode suppression in  $W$  allows rapid task switching, and that greater task-mode representations in  $W$  increase accuracy. These hypotheses are confirmed by forward simulation of the SC model (Fig. 3E). Thus, EPI produces novel, experimentally testable predictions: effective connectivity between these populations changes throughout learning, in a way that increases its task mode and decreases its side mode eigenvalues.

### 3.5 Characterizing biases in RNNs solving a posterior conditioning task

So far, each model we have studied was designed from fundamental biophysical principles, genetically- or functionally-defined neuron types. At a more abstract level of modeling, recurrent neural networks (RNNs) are high-dimensional dynamical models of computation and have become increasingly popular in neuroscience research [40]. Typically, RNNs are trained to do a task from a systems neuroscience experiment, and then the unit activations of the trained RNN are compared to recorded neural activity. Such highly parameterized nonlinear dynamical systems are challenging to characterize, let alone probabilistically infer. Predominantly, our understanding of RNN function comes from the identification of fixed points and their local linearized dynamics [47], yet these analyses do not afford a direct link between macroscopic connectivity parameters and dynamics. Alternatively, we use EPI to characterize the parameteric sources of solution bias in an RNN solving a toy mathematical problem.

Here, the task we consider is gaussian posterior conditioning: calculate the parameters of a gaussian posterior distribution on the mean of a gaussian likelihood  $\mu_y$ , given a single observation of  $y \sim \mathcal{N}(\mu_y, 1)$  and a prior  $p(\mu_y) = \mathcal{N}(4, 1)$  (Fig. 5A). The true posterior for an input of  $y = 2$  is  $p(\mu_y | y) = \mathcal{N}(3, 0.5)$ .

We used EPI to learn distributions of RNNs producing the correct posterior mean and variance in their mean activity  $\mu = \mu_{\text{post}}$  and temporal variance  $\Delta_T = \sigma_{\text{post}}^2$  (respectively), given an input of  $y = 2$ . (see Section A.2.4) (Fig. 5B).

Recent work establishes a link between RNN connectivity weights and the resulting dynamical re-

sponses of the network, using dynamic mean field theory (DMFT) [3]. Specifically, DMFT describes the properties of activity in infinite-size neural networks given a distribution on the connectivity weights. This theory has been extended from random neural networks to low-rank RNNs, which have low-dimensional parameterizations of RNN connectivity via the pairwise correlations of the low-rank vectors (i.e. the low-rank “geometry”) [23]. In such a model, the connectivity of a rank-1 RNN’s weight matrix  $J$  is the sum of a random component with strength determined by  $g$  and a structured component determined by the outer product of vectors  $m$  and  $n$ :

$$J = g\chi + \frac{1}{N}mn^\top, \quad (8)$$

where the activity  $x$  evolves as

$$\frac{dx}{dt} = -x(t) + J\phi(x(t)) + I(t), \quad (9)$$

and  $I(t)$  is some input,  $\phi$  is the tanh nonlinearity, and  $\chi_{ij} \sim \mathcal{N}(0, \frac{1}{N})$ . The entries of  $m$  and  $n$  are drawn from gaussian distributions  $m_i \sim \mathcal{N}(M_m, 1)$  and  $n_i \sim \mathcal{N}(M_n, 1)$ .

Mastrogiuseppe et al. designed low-rank connectivities via the pairwise correlations of the vectors  $m, n$  in models that solve tasks from behavioral neuroscience. We can consider the DMFT equation solver as a black box that takes in a low-rank parameterization  $z$  (e.g.  $z = [g, M_m, M_n]$ ) and outputs task-relevant response variables (e.g. average network activity  $\mu$ , the temporal variability in the network  $\Delta_T$ , or network activity along a given dimension  $\kappa$ ). Importantly, the solution produced by the solver is differentiable with respect to the input parameters, allowing us to combine DMFT with EPI to learn distributions on such connectivity parameters of RNNs that execute tasks via an emergent property defined on the task-relevant responses produced by DMFT.

When specifying the emergent property of gaussian posterior conditioning, we allowed a substantial amount of variability in the second moment constraints of the network mean  $\mu$  and temporal variance  $\Delta_T$ . This resulted in a distribution of rank-1 RNN parameterizations having a wide variety of biases in the resulting  $\mu_{\text{post}}$  and  $\sigma_{\text{post}}^2$  (under- or over-estimates of the posterior means and variances). We can examine the nature of the biases in this computation by visualizing the produced posterior means (Fig. 5B, left) and variances (Fig. 5B, right) in the EPI distribution. The inferred distribution has rough symmetry in the  $M_m$ - $M_n$  plane, suggesting a degeneracy in the product of  $M_m$  and  $M_n$  (Fig. 5B). The product of  $M_m$  and  $M_n$  almost completely determines the posterior mean (Fig. 5B, left), and the random strength  $g$  is the most influential variable on the temporal variance (Fig. 5B, right). Neither of these observations were obvious from the consistency equations afforded by DMFT (see Section A.2.4).

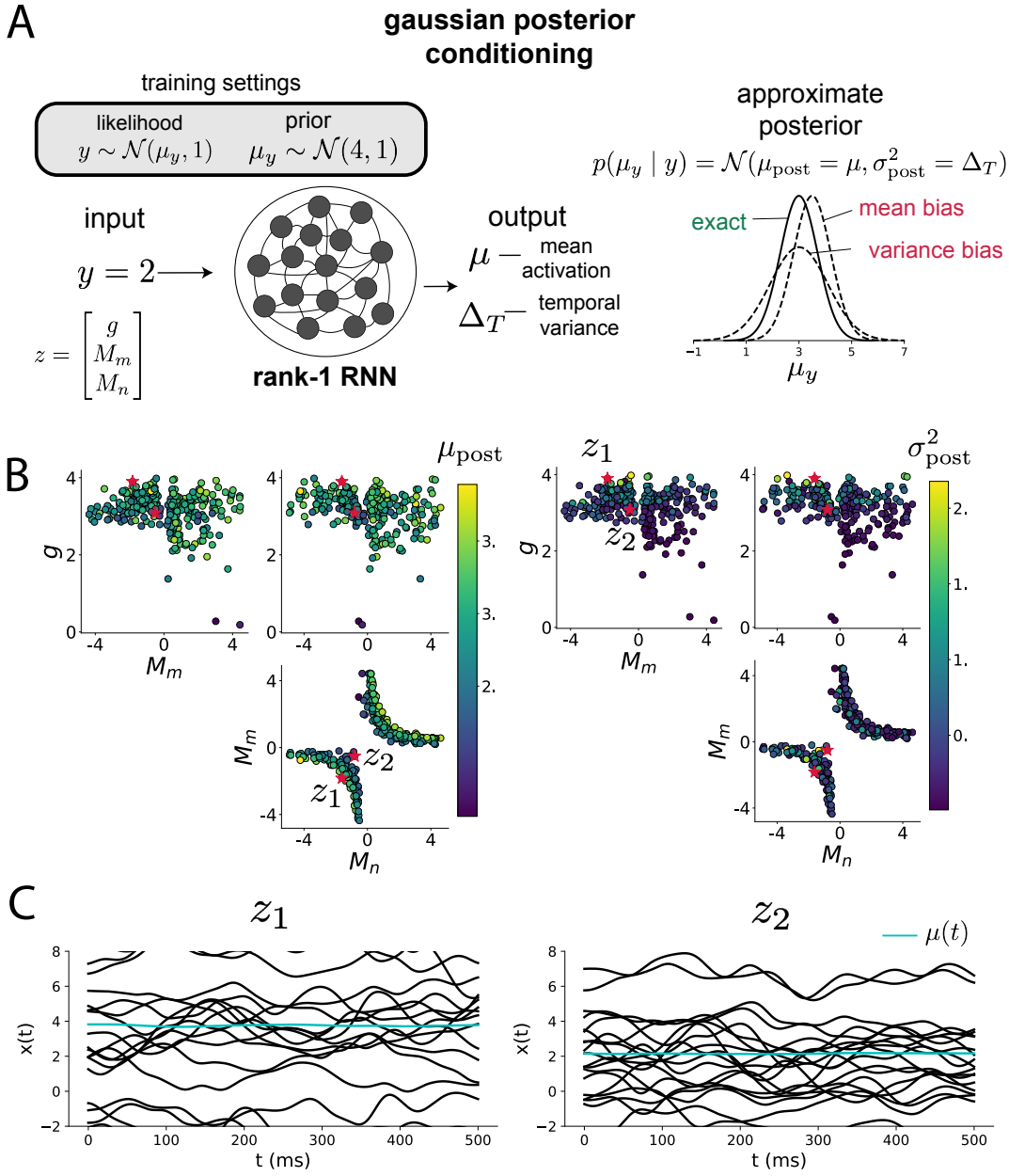


Figure 5: Sources of bias in RNN computation. A. (left) A rank-1 RNN running approximate Bayesian inference on  $\mu_y$  assuming a gaussian likelihood variance of 1 and a prior of  $\mathcal{N}(4, 1)$ . (center) The rank-1 RNN represents the computed gaussian posterior mean  $\mu_{\text{post}}$  and variance  $\sigma_{\text{post}}^2$  in its mean activity  $\mu$  and its temporal variance  $\Delta_T$ . (right) Bias in this computation can come from over- or under-estimating the posterior mean or variance. B. Distribution of rank-1 RNNs executing approximate Bayesian inference. Samples are colored by (left) posterior mean  $\mu_{\text{post}} = \mu$  and (right) posterior variance  $\sigma_{\text{post}}^2 = \Delta_T$ . C. Finite size realizations agree with the DMFT theory.

When working with DMFT, it's important to check that finite-size realizations of these infinite-size networks match the theoretical predictions. We check 2,000-neuron realizations of drawn parameters  $z_1$  and  $z_2$  from the inferred distribution.  $z_1$  has relatively high  $g$  and high  $M_m M_n$ , whereas  $z_2$  has relatively low  $g$  and low  $M_m M_n$ . Confirming our intuition,  $z_1$  overestimates the posterior mean, since mean activity  $\mu(t) > 3$  (Fig. 5C, left cyan). In turn,  $z_2$  underestimates the posterior mean, since  $\mu(t) < 3$  (Fig. 5C, right cyan). Finally,  $z_1$  results in evidently greater temporal variance than  $z_2$ . This novel procedure of doing inference in interpretable parameterizations of RNNs conditioned on task execution is straightforwardly generalizable to other tasks like noisy integration and context-dependent decision making (Fig. S1).

## 4 Discussion

### 4.1 EPI is a general tool for theoretical neuroscience

Models of biological systems are often comprised of complex nonlinear differential equations, making traditional theoretical analysis and statistical inference intractable. In contrast, EPI is capable of learning distributions of parameters in such models producing measurable signatures of computation. We have demonstrated its utility on biological models (STG), intermediate-level models of interacting genetically- and functionally-defined neuron-types (V1, SC), and the most abstract of models (RNNs). We are able to condition both deterministic and stochastic models on low-level emergent properties like firing rates of membrane potentials, as well as high-level cognitive function like gaussian posterior conditioning. Technically, EPI is tractable when the emergent property statistics are continuously differentiable with respect to the model parameters, which is very often the case; this emphasizes the general utility of EPI.

In this study, we have focused on applying EPI to low dimensional parameter spaces of models with low dimensional dynamical state. These choices were made to present the reader with a series of interpretable conclusions, which is more challenging in high dimensional spaces. In fact, EPI should scale reasonably to high dimensional parameter spaces, as the underlying technology has produced state-of-the-art performance on high-dimensional tasks such as texture generation [18]. Of course, increasing the dimensionality of the dynamical state of the model makes optimization more expensive, and there is a practical limit there as with any machine learning approach. For systems with high dimensional state, we recommend using theoretical approaches (e.g. [23]) to reason about reduced parameterizations of such high-dimensional systems.

364 There are additional technical considerations when assessing the suitability of EPI for a particu-  
365 lar modeling question. First and foremost, as in any optimization problem, the defined emergent  
366 property should always be appropriately conditioned (constraints should not have wildly different  
367 units). Furthermore, if the program is underconstrained (not enough constraints), the distribution  
368 grows (in entropy) unstably unless mapped to a finite support. If overconstrained, there is no pa-  
369 rameter set producing the emergent property, and EPI optimization will fail (appropriately). Next,  
370 one should consider the computational cost of the gradient calculations. In the best circumstance,  
371 there is a simple, closed form expression (e.g. Section A.1.1) for the emergent property statistic  
372 given the model parameters. On the other end of the spectrum, many forward simulation iterations  
373 may be required before a high quality measurement of the emergent property statistic is available  
374 (e.g. Section A.2.1). In such cases, optimization will be expensive.

## 375 4.2 Novel hypotheses from EPI

376 Machine learning has played an effective, multifaceted role in neuroscientific progress. Primarily,  
377 it has revealed structure in large-scale neural datasets [41, 42, 43, 44, 45, 46] (see review, [14]).  
378 Secondarily, trained algorithms of varying degrees of biological relevance are beginning to be viewed  
379 as fully-observable computational systems comparable to the brain [47, 48].

380 For example, consider the fact that we do not fully understand the four-dimensional models of V1  
381 [21]. Because analytical approaches to studying nonlinear dynamical systems become increasingly  
382 complicated when stepping from two-dimensional to three- or four-dimensional systems in the  
383 absence of restrictive simplifying assumptions [49], it is unsurprising that this model has been a  
384 challenge. In Section 3.3, we showed that EPI was far more informative about neuron-type input  
385 responsibility than the predictions afforded through analysis. By flexibly conditioning this V1 model  
386 on different emergent properties, we performed an exploratory analysis of a *model* rather than a  
387 dataset, which generated and proved out a set of testable predictions.

388 Of course, exploratory analyses can also be directed. For example, when interested in model  
389 changes during learning, one can use EPI to condition as we did in Section 3.4. This analysis  
390 identified experimentally testable predictions (proved out *in-silico*) of changes in connectivity in  
391 SC throughout learning. Precisely, we predict that an initial reduction in side mode eigenvalue,  
392 and a steady increase in task mode eigenvalue will take place, during learning, in the effective  
393 connectivity matrices of learning rats.

394 In our final analysis, we present a novel procedure for doing statistical inference on interpretable  
395 parameterizations of RNNs executing simple tasks . This methodology relies on recently extended  
396 theory of responses in random neural networks with minimal structure [23]. With this methodology,  
397 we can finally open the probabilistic model selection toolkit reasoning about the connectivity of  
398 RNNs solving tasks.

## 399 References

- 400 [1] Larry F Abbott. Theoretical neuroscience rising. *Neuron*, 60(3):489–495, 2008.
- 401 [2] John J Hopfield. Neural networks and physical systems with emergent collective computational  
402 abilities. *Proceedings of the national academy of sciences*, 79(8):2554–2558, 1982.
- 403 [3] Haim Sompolinsky, Andrea Crisanti, and Hans-Jurgen Sommers. Chaos in random neural  
404 networks. *Physical review letters*, 61(3):259, 1988.
- 405 [4] Misha V Tsodyks, William E Skaggs, Terrence J Sejnowski, and Bruce L McNaughton. Para-  
406 doxical effects of external modulation of inhibitory interneurons. *Journal of neuroscience*,  
407 17(11):4382–4388, 1997.
- 408 [5] Diederik P Kingma and Max Welling. Auto-encoding variational bayes. *International Confer-  
409 ence on Learning Representations*, 2014.
- 410 [6] Danilo Jimenez Rezende, Shakir Mohamed, and Daan Wierstra. Stochastic backpropagation  
411 and variational inference in deep latent gaussian models. *International Conference on Machine  
412 Learning*, 2014.
- 413 [7] Yuanjun Gao, Evan W Archer, Liam Paninski, and John P Cunningham. Linear dynamical  
414 neural population models through nonlinear embeddings. In *Advances in neural information  
415 processing systems*, pages 163–171, 2016.
- 416 [8] Yuan Zhao and Il Memming Park. Recursive variational bayesian dual estimation for nonlinear  
417 dynamics and non-gaussian observations. *stat*, 1050:27, 2017.
- 418 [9] Gabriel Barello, Adam Charles, and Jonathan Pillow. Sparse-coding variational auto-encoders.  
419 *bioRxiv*, page 399246, 2018.

- [10] Chethan Pandarinath, Daniel J O’Shea, Jasmine Collins, Rafal Jozefowicz, Sergey D Stavisky, Jonathan C Kao, Eric M Trautmann, Matthew T Kaufman, Stephen I Ryu, Leigh R Hochberg, et al. Inferring single-trial neural population dynamics using sequential auto-encoders. *Nature methods*, page 1, 2018.
- [11] Alexander B Wiltschko, Matthew J Johnson, Giuliano Iurilli, Ralph E Peterson, Jesse M Katon, Stan L Pashkovski, Victoria E Abraira, Ryan P Adams, and Sandeep Robert Datta. Mapping sub-second structure in mouse behavior. *Neuron*, 88(6):1121–1135, 2015.
- [12] Matthew J Johnson, David K Duvenaud, Alex Wiltschko, Ryan P Adams, and Sandeep R Datta. Composing graphical models with neural networks for structured representations and fast inference. In *Advances in neural information processing systems*, pages 2946–2954, 2016.
- [13] Eleanor Batty, Matthew Whiteway, Shreya Saxena, Dan Biderman, Taiga Abe, Simon Musall, Winthrop Gillis, Jeffrey Markowitz, Anne Churchland, John Cunningham, et al. Behavenet: nonlinear embedding and bayesian neural decoding of behavioral videos. *Advances in Neural Information Processing Systems*, 2019.
- [14] Liam Paninski and John P Cunningham. Neural data science: accelerating the experiment-analysis-theory cycle in large-scale neuroscience. *Current opinion in neurobiology*, 50:232–241, 2018.
- [15] Danilo Jimenez Rezende and Shakir Mohamed. Variational inference with normalizing flows. *International Conference on Machine Learning*, 2015.
- [16] Laurent Dinh, Jascha Sohl-Dickstein, and Samy Bengio. Density estimation using real nvp. *arXiv preprint arXiv:1605.08803*, 2016.
- [17] George Papamakarios, Theo Pavlakou, and Iain Murray. Masked autoregressive flow for density estimation. In *Advances in Neural Information Processing Systems*, pages 2338–2347, 2017.
- [18] Gabriel Loaiza-Ganem, Yuanjun Gao, and John P Cunningham. Maximum entropy flow networks. *International Conference on Learning Representations*, 2017.
- [19] Dustin Tran, Rajesh Ranganath, and David Blei. Hierarchical implicit models and likelihood-free variational inference. In *Advances in Neural Information Processing Systems*, pages 5523–5533, 2017.

- [20] Gabrielle J Gutierrez, Timothy O’Leary, and Eve Marder. Multiple mechanisms switch an electrically coupled, synaptically inhibited neuron between competing rhythmic oscillators. *Neuron*, 77(5):845–858, 2013.
- [21] Ashok Litwin-Kumar, Robert Rosenbaum, and Brent Doiron. Inhibitory stabilization and visual coding in cortical circuits with multiple interneuron subtypes. *Journal of neurophysiology*, 115(3):1399–1409, 2016.
- [22] Chunyu A Duan, Marino Pagan, Alex T Piet, Charles D Kopec, Athena Akrami, Alexander J Riordan, Jeffrey C Erlich, and Carlos D Brody. Collicular circuits for flexible sensorimotor routing. *bioRxiv*, page 245613, 2018.
- [23] Francesca Mastrogiovanni and Srdjan Ostojic. Linking connectivity, dynamics, and computations in low-rank recurrent neural networks. *Neuron*, 99(3):609–623, 2018.
- [24] Sean R Bittner, Agostina Palmigiano, Kenneth D Miller, and John P Cunningham. Degenerate solution networks for theoretical neuroscience. *Computational and Systems Neuroscience Meeting (COSYNE), Lisbon, Portugal*, 2019.
- [25] Sean R Bittner, Alex T Piet, Chunyu A Duan, Agostina Palmigiano, Kenneth D Miller, Carlos D Brody, and John P Cunningham. Examining models in theoretical neuroscience with degenerate solution networks. *Bernstein Conference*, 2019.
- [26] Jan-Matthis Lueckmann, Pedro Goncalves, Chaitanya Chintaluri, William F Podlaski, Giacomo Bassetto, Tim P Vogels, and Jakob H Macke. Amortised inference for mechanistic models of neural dynamics. In *Computational and Systems Neuroscience Meeting (COSYNE), Lisbon, Portugal*, 2019.
- [27] Eve Marder and Vatsala Thirumalai. Cellular, synaptic and network effects of neuromodulation. *Neural Networks*, 15(4-6):479–493, 2002.
- [28] Astrid A Prinz, Dirk Bucher, and Eve Marder. Similar network activity from disparate circuit parameters. *Nature neuroscience*, 7(12):1345, 2004.
- [29] Edwin T Jaynes. Information theory and statistical mechanics. *Physical review*, 106(4):620, 1957.
- [30] Gamaleldin F Elsayed and John P Cunningham. Structure in neural population recordings: an expected byproduct of simpler phenomena? *Nature neuroscience*, 20(9):1310, 2017.

- 477 [31] Cristina Savin and Gašper Tkačik. Maximum entropy models as a tool for building precise  
478 neural controls. *Current opinion in neurobiology*, 46:120–126, 2017.
- 479 [32] Brendan K Murphy and Kenneth D Miller. Balanced amplification: a new mechanism of  
480 selective amplification of neural activity patterns. *Neuron*, 61(4):635–648, 2009.
- 481 [33] Hirofumi Ozeki, Ian M Finn, Evan S Schaffer, Kenneth D Miller, and David Ferster. Inhibitory  
482 stabilization of the cortical network underlies visual surround suppression. *Neuron*, 62(4):578–  
483 592, 2009.
- 484 [34] Daniel B Rubin, Stephen D Van Hooser, and Kenneth D Miller. The stabilized supralinear  
485 network: a unifying circuit motif underlying multi-input integration in sensory cortex. *Neuron*,  
486 85(2):402–417, 2015.
- 487 [35] Henry Markram, Maria Toledo-Rodriguez, Yun Wang, Anirudh Gupta, Gilad Silberberg, and  
488 Caizhi Wu. Interneurons of the neocortical inhibitory system. *Nature reviews neuroscience*,  
489 5(10):793, 2004.
- 490 [36] Bernardo Rudy, Gordon Fishell, SooHyun Lee, and Jens Hjerling-Leffler. Three groups of  
491 interneurons account for nearly 100% of neocortical gabaergic neurons. *Developmental neuro-  
492 biology*, 71(1):45–61, 2011.
- 493 [37] (2018) Allen Institute for Brain Science. Layer 4 model of v1. available from:  
494 <https://portal.brain-map.org/explore/models/l4-mv1>.
- 495 [38] Yazan N Billeh, Binghuang Cai, Sergey L Gratiy, Kael Dai, Ramakrishnan Iyer, Nathan W  
496 Gouwens, Reza Abbasi-Asl, Xiaoxuan Jia, Joshua H Siegle, Shawn R Olsen, et al. Systematic  
497 integration of structural and functional data into multi-scale models of mouse primary visual  
498 cortex. *bioRxiv*, page 662189, 2019.
- 499 [39] Chunyu A Duan, Jeffrey C Erlich, and Carlos D Brody. Requirement of prefrontal and midbrain  
500 regions for rapid executive control of behavior in the rat. *Neuron*, 86(6):1491–1503, 2015.
- 501 [40] Omri Barak. Recurrent neural networks as versatile tools of neuroscience research. *Current  
502 opinion in neurobiology*, 46:1–6, 2017.
- 503 [41] Robert E Kass and Valérie Ventura. A spike-train probability model. *Neural computation*,  
504 13(8):1713–1720, 2001.

- 505 [42] Emery N Brown, Loren M Frank, Dengda Tang, Michael C Quirk, and Matthew A Wilson.  
506 A statistical paradigm for neural spike train decoding applied to position prediction from  
507 ensemble firing patterns of rat hippocampal place cells. *Journal of Neuroscience*, 18(18):7411–  
508 7425, 1998.
- 509 [43] Liam Paninski. Maximum likelihood estimation of cascade point-process neural encoding  
510 models. *Network: Computation in Neural Systems*, 15(4):243–262, 2004.
- 511 [44] M Yu Byron, John P Cunningham, Gopal Santhanam, Stephen I Ryu, Krishna V Shenoy, and  
512 Maneesh Sahani. Gaussian-process factor analysis for low-dimensional single-trial analysis  
513 of neural population activity. In *Advances in neural information processing systems*, pages  
514 1881–1888, 2009.
- 515 [45] Kenneth W Latimer, Jacob L Yates, Miriam LR Meister, Alexander C Huk, and Jonathan W  
516 Pillow. Single-trial spike trains in parietal cortex reveal discrete steps during decision-making.  
517 *Science*, 349(6244):184–187, 2015.
- 518 [46] Lea Duncker, Gergo Bohner, Julien Boussard, and Maneesh Sahani. Learning interpretable  
519 continuous-time models of latent stochastic dynamical systems. *Proceedings of the 36th Inter-*  
520 *national Conference on Machine Learning*, 2019.
- 521 [47] David Sussillo and Omri Barak. Opening the black box: low-dimensional dynamics in high-  
522 dimensional recurrent neural networks. *Neural computation*, 25(3):626–649, 2013.
- 523 [48] Blake A Richards and et al. A deep learning framework for neuroscience. *Nature Neuroscience*,  
524 2019.
- 525 [49] Steven H Strogatz. Nonlinear dynamics and chaos: with applications to physics. *Biology,*  
526 *Chemistry, and Engineering (Studies in Nonlinearity)*, Perseus, Cambridge, UK, 1994.
- 527 [50] Rajesh Ranganath, Sean Gerrish, and David Blei. Black box variational inference. In *Artificial*  
528 *Intelligence and Statistics*, pages 814–822, 2014.
- 529 [51] Martin J Wainwright, Michael I Jordan, et al. Graphical models, exponential families, and  
530 variational inference. *Foundations and Trends® in Machine Learning*, 1(1–2):1–305, 2008.
- 531 [52] Laurent Dinh, Jascha Sohl-Dickstein, and Samy Bengio. Density estimation using real nvp.  
532 *Proceedings of the 5th International Conference on Learning Representations*, 2017.

- 533 [53] Carsten K Pfeffer, Mingshan Xue, Miao He, Z Josh Huang, and Massimo Scanziani. Inhi-  
 534 bition of inhibition in visual cortex: the logic of connections between molecularly distinct  
 535 interneurons. *Nature Neuroscience*, 16(8):1068, 2013.

536 **A Methods**

537 **A.1 Emergent property inference (EPI)**

538 Emergent property inference (EPI) learns distributions of theoretical model parameters that pro-  
 539 duce emergent properties of interest. EPI combines ideas from likelihood-free variational inference  
 540 [19] and maximum entropy flow networks [18]. A maximum entropy flow network is used as a deep  
 541 probability distribution for the parameters, while these samples often parameterize a differentiable  
 542 model simulator, which may lack a tractable likelihood function.

543 Consider model parameterization  $z$  and data  $x$  generated from some theoretical model simulator  
 544 represented as  $p(x | z)$ , which may be deterministic or stochastic. Theoretical models usually have  
 545 known sampling procedures for simulating activity given a circuit parameterization, yet often lack  
 546 an explicit likelihood function due to the nonlinearities and dynamics. With EPI, a distribution  
 547 on parameters  $z$  is learned, that yields an emergent property of interest  $\mathcal{B}$ ,

$$\mathcal{B} \leftrightarrow E_{z \sim q_\theta} [E_{x \sim p(x|z)} [T(x)]] = \mu \quad (10)$$

548 by making an approximation  $q_\theta(z)$  to  $p(z | \mathcal{B})$  (see Section A.1.5). So, over the DSN distribution  
 549  $q_\theta(z)$  of model  $p(x | z)$  for behavior  $\mathcal{B}$ , the emergent properties  $T(x)$  are constrained in expectation  
 550 to  $\mu$ .

551 In deep probability distributions, a simple random variable  $w \sim p_0$  is mapped deterministically  
 552 via a function  $f_\theta$  parameterized by a neural network to the support of the distribution of interest  
 553 where  $z = f_\theta(w) = f_l(\dots f_1(w))$ . Given a theoretical model  $p(x | z)$  and some behavior of interest  
 554  $\mathcal{B}$ , the deep probability distributions are trained by optimizing the neural network parameters  $\theta$  to  
 555 find a good approximation  $q_\theta^*$  within the deep variational family  $Q$  to  $p(z | \mathcal{B})$ .

556 In most settings (especially those relevant to theoretical neuroscience) the likelihood of the behavior  
 557 with respect to the model parameters  $p(T(x) | z)$  is unknown or intractable, requiring an alternative  
 558 to stochastic gradient variational Bayes [5] or black box variational inference[50]. These types  
 559 of methods called likelihood-free variational inference (LFVI, [19]) skate around the intractable  
 560 likelihood function in situations where there is a differentiable simulator. Akin to LFVI, DSNs are

561 optimized with the following objective for a given theoretical model, emergent property statistics  
 562  $T(x)$ , and emergent property constraints  $\mu$ :

$$\begin{aligned} q_\theta^*(z) &= \underset{q_\theta \in Q}{\operatorname{argmax}} H(q_\theta(z)) \\ \text{s.t. } E_{z \sim q_\theta} [E_{x \sim p(x|z)} [T(x)]] &= \mu \end{aligned} \quad (11)$$

563 Optimizing this objective is a technological accomplishment in its own right, the details of which  
 564 we elaborate in Section A.1.2. Before going through those details, we ground this optimization in  
 565 a toy example.

566 **A.1.1 Example: 2D LDS**

567 To gain intuition for EPI, consider two-dimensional linear dynamical systems,  $\tau \dot{x} = Ax$  with

$$A = \begin{bmatrix} a_1 & a_2 \\ a_3 & a_4 \end{bmatrix}$$

568 that produce a band of oscillations. To do EPI with the dynamics matrix elements as the free  
 569 parameters  $z = [a_1, a_2, a_3, a_4]$ , and fixing  $\tau = 1$ , such that the posterior yields a band of oscillations,  
 570 the emergent property statistics  $T(x)$  are chosen to contain the first- and second-moments of the  
 571 oscillatory frequency  $\Omega$  and the growth/decay factor  $d$  of the oscillating system. To learn the  
 572 distribution of real entries of  $A$  that yield a distribution of  $d$  with mean zero with variance  $0.25^2$ ,  
 573 and oscillation frequency  $\Omega$  with mean 1 Hz with variance  $(0.1\text{Hz})^2$ , then we would select the real  
 574 part of the complex conjugate eigenvalues  $\operatorname{real}(\lambda_1) = d$  (via an arbitrary choice of eigenvalue of the  
 575 dynamics matrix  $\lambda_1$ ) and the positive imaginary component of one of the eigenvalues  $\operatorname{imag}(\lambda_1) =$   
 576  $2\pi\Omega$  as the emergent property statistics. Those emergent property statistics are then constrained  
 577 to

$$\mu = E \begin{bmatrix} \operatorname{real}(\lambda_1) \\ \operatorname{imag}(\lambda_1) \\ (\operatorname{real}(\lambda_1) - 0)^2 \\ (\operatorname{imag}(\lambda_1) - 2\pi\Omega)^2 \end{bmatrix} = \begin{bmatrix} 0.0 \\ 2\pi\Omega \\ 0.25^2 \\ (2\pi 0.1)^2 \end{bmatrix} \quad (12)$$

578 where  $\Omega = 1\text{Hz}$ . Unlike the models we study in the paper which calculate  $E_{x \sim p(x|z)} [T(x)]$  via  
 579 forward simulation, we have a closed form for the eigenvalues of the dynamics matrix.  $\lambda$  can be  
 580 calculated using the quadratic formula:

$$\lambda = \frac{\left(\frac{a_1+a_4}{\tau}\right) \pm \sqrt{\left(\frac{a_1+a_4}{\tau}\right)^2 + 4\left(\frac{a_2a_3-a_1a_4}{\tau}\right)}}{2} \quad (13)$$

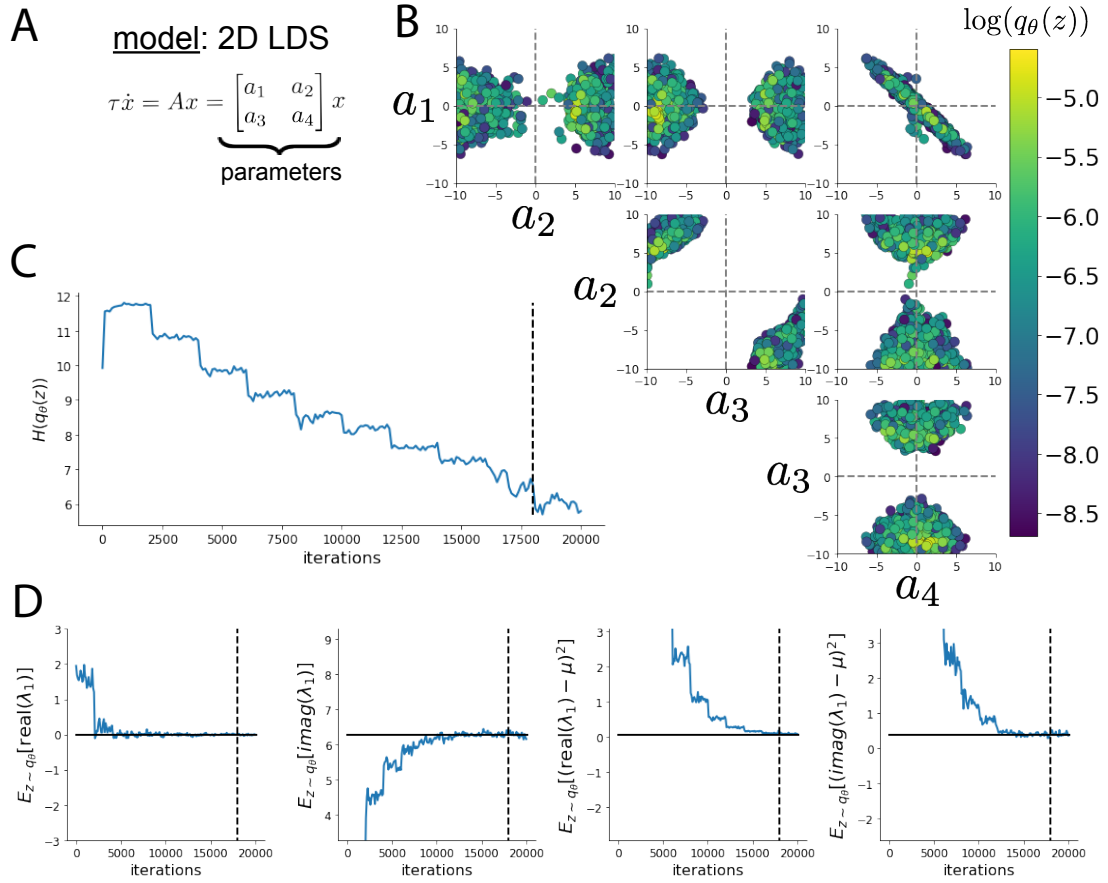


Fig. S2: A. Two-dimensional linear dynamical system model, where real entries of the dynamics matrix  $A$  are the parameters. B. The DSN distribution for a 2D LDS with  $\tau = 1$  that produces an average of 1Hz oscillations with some small amount of variance. C. Entropy throughout the optimization. At the beginning of each augmented Lagrangian epoch (5,000 iterations), the entropy dips due to the shifted optimization manifold where emergent property constraint satisfaction is increasingly weighted. D. Emergent property moments throughout optimization. At the beginning of each augmented Lagrangian epoch, the emergent property moments move closer to their constraints.

581 where  $\lambda_1$  is the eigenvalue of  $\frac{1}{\tau}A$  with greatest real part. Even though  $E_{x \sim p(x|z)}[T(x)]$  is calculable  
 582 directly via a closed form function and does not require simulation, we cannot derive the distribution  
 583  $q_\theta^*$  directly. This is due to the formally hard problem of the backward mapping: finding the natural  
 584 parameters  $\eta$  from the mean parameters  $\mu$  of an exponential family distribution [51]. Instead, we  
 585 can use EPI to learn the linear system parameters producing such a band of oscillations (Fig. S2B).  
 586 Even this relatively simple system has nontrivial (though intuitively sensible) structure in the  
 587 parameter distribution. To validate our method (further than that of the underlying technology  
 588 on a ground truth solution [18]) we can analytically derive the contours of the probability density  
 589 from the emergent property statistics and values (Fig. S3). In the  $a_1 - a_4$  plane, is a black line  
 590 at  $\text{real}(\lambda_1) = \frac{a_1+a_4}{2} = 0$ , a dotted black line at the standard deviation  $\text{real}(\lambda_1) = \frac{a_1+a_4}{2} \pm 1$ , and a  
 591 grey line at twice the standard deviation  $\text{real}(\lambda_1) = \frac{a_1+a_4}{2} \pm 2$  (Fig. S3A). Here the lines denote the  
 592 set of solutions at fixed behaviors, which overlay the posterior obtained through EPI. The learned  
 593 DSN distribution precisely reflects the desired statistical constraints and model degeneracy in the  
 594 sum of  $a_1$  and  $a_4$ . Intuitively, the parameters equivalent with respect to emergent property statistic  
 595  $\text{real}(\lambda_1)$  have similar log densities.

596 To explain the structure in the bimodality of the DSN posterior, we can look at the imaginary  
 597 component of  $\lambda_1$ . When  $\text{real}(\lambda_1) = \frac{a_1+a_4}{2} = 0$ , we have

$$\text{imag}(\lambda_1) = \begin{cases} \sqrt{\frac{a_1a_4-a_2a_3}{\tau}}, & \text{if } a_1a_4 < a_2a_3 \\ 0 & \text{otherwise} \end{cases} \quad (14)$$

598 When  $\tau = 1$  and  $a_1a_4 > a_2a_3$  (center of distribution above), we have the following equation for the  
 599 other two dimensions:

$$\text{imag}(\lambda_1)^2 = a_1a_4 - a_2a_3 \quad (15)$$

600 Since we constrained  $E_{q_\theta}[\text{imag}(\lambda)] = 2\pi$  (with  $\omega = 1$ ), we can plot contours of the equation  
 601  $\text{imag}(\lambda_1)^2 = a_1a_4 - a_2a_3 = (2\pi)^2$  for various  $a_1a_4$  (Fig. S3A). If  $\sigma_{1,4} = E_{q_\theta}(|a_1a_4 - E_{q_\theta}[a_1a_4]|)$ ,  
 602 then we plot the contours as  $a_1a_4 = 0$  (black),  $a_1a_4 = -\sigma_{1,4}$  (black dotted), and  $a_1a_4 = -2\sigma_{1,4}$   
 603 (grey dotted) (Fig. S3B). This validates the curved structure of the inferred distribution learned  
 604 through EPI. We take steps in negative standard deviation of  $a_1a_4$  (dotted and gray lines), since  
 605 there are few positive values  $a_1a_4$  in the posterior. Subtler model-behavior combinations will have  
 606 even more complexity, further motivating the use of EPI for understanding these systems. Indeed,  
 607 we sample a distribution of systems oscillating near 1Hz (Fig. S4).

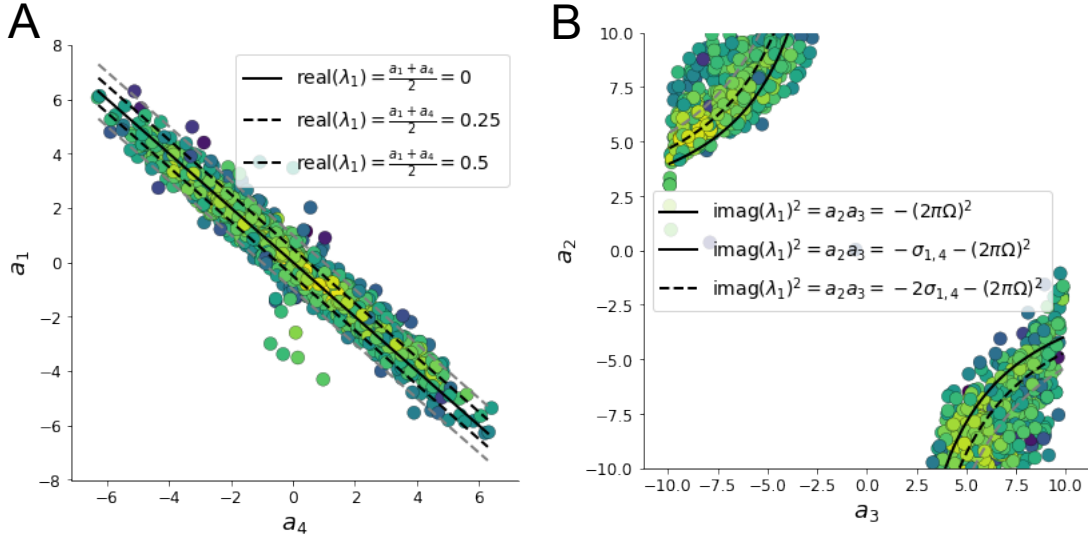


Fig. S3: A. Probability contours in the  $a_1 - a_4$  plane can be derived from the relationship to emergent property statistic of growth/decay factor. B. Probability contours in the  $a_2 - a_3$  plane can be derived from relationship to the emergent property statistic of oscillation frequency.

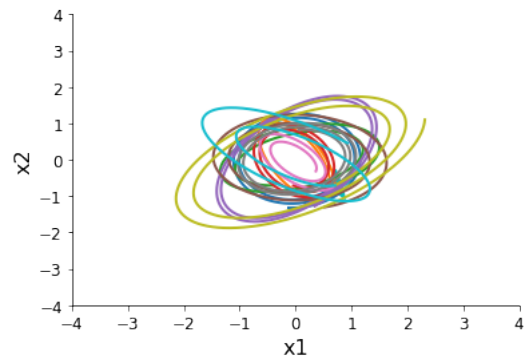


Fig. S4: Sampled dynamical system trajectories from the EPI distribution. Each trajectory is initialized at  $x(0) = \left[ \frac{\sqrt{2}}{2} \quad -\frac{\sqrt{2}}{2} \right]$ .

608 **A.1.2 Augmented Lagrangian optimization**

609 To optimize  $q_\theta(z)$  in equation 1, the constrained optimization is performed using the augmented  
 610 Lagrangian method. The following objective is minimized:

$$L(\theta; \alpha, c) = -H(q_\theta) + \alpha^\top \delta(\theta) + \frac{c}{2} \|\delta(\theta)\|^2 \quad (16)$$

611 where  $\delta(\theta) = E_{z \sim q_\theta} [E_{x \sim p(x|z)} [T(x) - \mu]]$ ,  $\alpha \in \mathcal{R}^m$  are the Lagrange multipliers and  $c$  is the penalty  
 612 coefficient. For a fixed  $(\alpha, c)$ ,  $\theta$  is optimized with stochastic gradient descent. A low value of  $c$  is  
 613 used initially, and increased during each augmented Lagrangian epoch – a period of optimization  
 614 with fixed  $\alpha$  and  $c$  for a given number of stochastic optimization iterations. Similarly,  $\alpha$  is tuned  
 615 each epoch based on the constraint violations. For the linear 2-dimensional system (Fig. S2C)  
 616 optimization hyperparameters are initialized to  $c_1 = 10^{-4}$  and  $\alpha_1 = 0$ . The penalty coefficient  
 617 is updated based on a hypothesis test regarding the reduction in constraint violation. The p-  
 618 value of  $E[\|\delta(\theta_{k+1})\|] > \gamma E[\|\delta(\theta_k)\|]$  is computed, and  $c_{k+1}$  is updated to  $\beta c_k$  with probability  
 619  $1 - p$ . Throughout the project,  $\beta = 4.0$  and  $\gamma = 0.25$  is used. The other update rule is  $\alpha_{k+1} =$   
 620  $\alpha_k + c_k \frac{1}{n} \sum_{i=1}^n (T(x^{(i)}) - \mu)$ . In this example, each augmented Lagrangian epoch ran for 2,000  
 621 iterations. We consider the optimization to have converged when a null hypothesis test of constraint  
 622 violations being zero is accepted for all constraints at a significance threshold 0.05. This is the dotted  
 623 line on the plots below depicting the optimization cutoff of EPI optimization for the 2-dimensional  
 624 linear system. If the optimization is left to continue running, entropy usually decreases, and  
 625 structural pathologies in the distribution may be introduced.

626 The intention is that  $c$  and  $\alpha$  start at values encouraging entropic growth early in optimization.  
 627 Then, as they increase in magnitude with each training epoch, the constraint satisfaction terms are  
 628 increasingly weighted, resulting in a decrease in entropy. Rather than using a naive initialization,  
 629 before EPI, we optimize the deep probability distribution parameters to generate samples of an  
 630 isotropic gaussian of a selected variance, such as 1.0 for the 2D LDS example. This provides a  
 631 convenient starting point, whose level of entropy is controlled by the user.

632 **A.1.3 Normalizing flows**

633 Since we are optimizing parameters  $\theta$  of our deep probability distribution with respect to the  
 634 entropy, we will need to take gradients with respect to the log-density of samples from the deep  
 635 probability distribution.

$$H(q_\theta(z)) = \int -q_\theta(z) \log(q_\theta(z)) dz = E_{z \sim q_\theta} [-\log(q_\theta(z))] = E_{\omega \sim q_0} [-\log(q_\theta(f_\theta(\omega)))] \quad (17)$$

636

$$\nabla_\theta H(q_\theta(z)) = E_{\omega \sim q_0} [-\nabla_\theta \log(q_\theta(f_\theta(\omega)))] \quad (18)$$

- 637 Deep probability models typically consist of several layers of fully connected neural networks.  
 638 When each neural network layer is restricted to be a bijective function, the sample density can be  
 639 calculated using the change of variables formula at each layer of the network. For  $z' = f(z)$ ,

$$q(z') = q(f^{-1}(z')) \left| \det \frac{\partial f^{-1}(z')}{\partial z'} \right| = q(z) \left| \det \frac{\partial f(z)}{\partial z} \right|^{-1} \quad (19)$$

- 640 However, this computation has cubic complexity in dimensionality for fully connected layers. By  
 641 restricting our layers to normalizing flows [15] – bijective functions with fast log determinant ja-  
 642 cobian computations, we can tractably optimize deep generative models with objectives that are a  
 643 function of sample density, like entropy. Most of our analyses use real NVP [52], which have proven  
 644 effective in our architecture searches, and have the advantageous features of fast sampling and fast  
 645 density evaluation.

646 **A.1.4 Related work**

647 (To come)

648

649 **A.1.5 Emergent property inference as variational inference in an exponential family**

650 (To come)

651

652 **A.2 Theoretical models**

- 653 In this study, we used emergent property inference to examine several models relevant to theoretical  
 654 neuroscience. Here, we provide the details of each model and the related analyses.

655 **A.2.1 Stomatogastric ganglion**

656 Each neuron's membrane potential  $x_m(t)$  is the solution of the following differential equation.

$$C_m \frac{dx_m}{dt} = -[h_{leak}(x; z) + h_{Ca}(x; z) + h_K(x; z) + h_{hyp}(x; z) + h_{elec}(x; z) + h_{syn}(x; z)] \quad (20)$$

657 The membrane potential of each neuron is affected by the leak, calcium, potassium, hyperpolariza-  
 658 tion, electrical and synaptic currents, respectively. The capacitance of the cell membrane was set to  
 659  $C_m = 1nF$ . Each current is a function of the neuron's membrane potential  $x_m$  and the parameters  
 660 of the circuit such as  $g_{el}$  and  $g_{syn}$ , whose effect on the circuit is considered in the motivational  
 661 example of EPI in Fig. 1. Specifically, the currents are the difference in the neuron's membrane  
 662 potential and that current type's reversal potential multiplied by a conductance:

$$h_{leak}(x; z) = g_{leak}(x_m - V_{leak}) \quad (21)$$

$$h_{elec}(x; z) = g_{el}(x_m^{post} - x_m^{pre}) \quad (22)$$

$$h_{syn}(x; z) = g_{syn}S_\infty^{pre}(x_m^{post} - V_{syn}) \quad (23)$$

$$h_{Ca}(x; z) = g_{Ca}M_\infty(x_m - V_{Ca}) \quad (24)$$

$$h_K(x; z) = g_KN(x_m - V_K) \quad (25)$$

$$h_{hyp}(x; z) = g_hH(x_m - V_{hyp}) \quad (26)$$

668 The reversal potentials were set to  $V_{leak} = -40mV$ ,  $V_{Ca} = 100mV$ ,  $V_K = -80mV$ ,  $V_{hyp} = -20mV$ ,  
 669 and  $V_{syn} = -75mV$ . The other conductance parameters were fixed to  $g_{leak} = 1 \times 10^{-4}\mu S$ .  $g_{Ca}$ ,  
 670  $g_K$ , and  $g_{hyp}$  had different values based on fast, intermediate (hub) or slow neuron. Fast:  $g_{Ca} =$   
 671  $1.9 \times 10^{-2}$ ,  $g_K = 3.9 \times 10^{-2}$ , and  $g_{hyp} = 2.5 \times 10^{-2}$ . Intermediate:  $g_{Ca} = 1.7 \times 10^{-2}$ ,  $g_K = 1.9 \times 10^{-2}$ ,  
 672 and  $g_{hyp} = 8.0 \times 10^{-3}$ . Intermediate:  $g_{Ca} = 8.5 \times 10^{-3}$ ,  $g_K = 1.5 \times 10^{-2}$ , and  $g_{hyp} = 1.0 \times 10^{-2}$ .

673 Furthermore, the Calcium, Potassium, and hyperpolarization channels have time-dependent gating  
 674 dynamics dependent on steady-state gating variables  $M_\infty$ ,  $N_\infty$  and  $H_\infty$ , respectively.

$$M_\infty = 0.5 \left( 1 + \tanh \left( \frac{x_m - v_1}{v_2} \right) \right) \quad (27)$$

$$\frac{dN}{dt} = \lambda_N(N_\infty - N) \quad (28)$$

$$N_\infty = 0.5 \left( 1 + \tanh \left( \frac{x_m - v_3}{v_4} \right) \right) \quad (29)$$

$$\lambda_N = \phi_N \cosh \left( \frac{x_m - v_3}{2v_4} \right) \quad (30)$$

678

$$\frac{dH}{dt} = \frac{(H_\infty - H)}{\tau_h} \quad (31)$$

679

$$H_\infty = \frac{1}{1 + \exp\left(\frac{x_m + v_5}{v_6}\right)} \quad (32)$$

680

$$\tau_h = 272 - \left( \frac{-1499}{1 + \exp\left(\frac{-x_m + v_7}{v_8}\right)} \right) \quad (33)$$

681 where we set  $v_1 = 0mV$ ,  $v_2 = 20mV$ ,  $v_3 = 0mV$ ,  $v_4 = 15mV$ ,  $v_5 = 78.3mV$ ,  $v_6 = 10.5mV$ ,  
 682  $v_7 = -42.2mV$ ,  $v_8 = 87.3mV$ ,  $v_9 = 5mV$ , and  $v_{th} = -25mV$ . These are the same parameter  
 683 values used in [20].

684 Finally, there is a synaptic gating variable as well:

$$S_\infty = \frac{1}{1 + \exp\left(\frac{v_{th} - x_m}{v_9}\right)} \quad (34)$$

685 When the dynamic gating variables are considered, this is actually a 15-dimensional nonlinear  
 686 dynamical system.

687 In order to measure the frequency of the hub neuron during EPI, the STG model was simulated  
 688 for  $T = 500$  time steps of  $dt = 25ms$ . In EPI, since gradients are taken through the simulation  
 689 process, the number of time steps are kept as modest if possible. The chosen  $dt$  and  $T$  were the  
 690 most computationally convenient choices yielding accurate frequency measurement.

691 Our original approach to measuring frequency was to take the max of the fast Fourier transform  
 692 (FFT) of the simulated time series. There are a few key considerations here. One is resolution  
 693 in frequency space. Each FFT entry will correspond to a signal frequency of  $\frac{F_s k}{N}$ , where  $N$  is  
 694 the number of samples used for the FFT,  $F_s = \frac{1}{dt}$ , and  $k \in [0, 1, \dots, N - 1]$ . Our resolution is  
 695 improved by increasing  $N$  and decreasing  $dt$ . Increasing  $N = T - b$ , where  $b$  is some fixed number  
 696 of buffer burn-in initialization samples, necessitates an increase in simulation time steps  $T$ , which  
 697 directly increases computational cost. Increasing  $F_s$  (decreasing  $dt$ ) increases system approximation  
 698 accuracy, but requires more time steps before a full cycle is observed. At the level of  $dt = 0.025$ ,  
 699 thousands of temporal samples were required for resolution of .01Hz. These challenges in frequency  
 700 resolution with the discrete Fourier transform motivated the use of an alternative basis of complex  
 701 exponentials. Instead, we used a basis of complex exponentials with frequencies from 0.0-1.0 Hz at  
 702 0.01Hz resolution,  $\Phi = [0.0, 0.01, \dots, 1.0]^\top$

703 Another consideration was that the frequency spectra of the hub neuron has several peaks. This  
 704 was due to high-frequency sub-threshold activity. The maximum frequency was often not the firing

frequency. Accordingly, subthreshold activity was set to zero, and the whole signal was low-pass filtered with a moving average window of length 20. The signal was subsequently mean centered. After this pre-processing, the maximum frequency in the filter bank accurately reflected the firing frequency.

Finally, to differentiate through the maximum frequency identification step, we used a sum-of-powers normalization strategy: Let  $\mathcal{X}_i \in \mathcal{C}^{|\Phi|}$  be the complex exponential filter bank dot products with the signal  $x_i \in \mathcal{R}^N$ , where  $i \in \{\text{f1}, \text{f2}, \text{hub}, \text{s1}, \text{s2}\}$ . The “frequency identification” vector is

$$u_i = \frac{|\mathcal{X}_i|^\alpha}{\sum_{k=1}^N |\mathcal{X}_i(k)|^\alpha} \quad (35)$$

The frequency is then calculated as  $\Omega_i = u_i^\top \Phi$  with  $\alpha = 100$ .

Network syncing, like all other emergent properties in this work, are defined by the emergent property statistics and values. The emergent property statistics are the first- and second-moments of the firing frequencies. The first moments are set to 0.55Hz, while the second moments are set to  $0.025\text{Hz}^2$ .

$$E \begin{bmatrix} \Omega_{\text{f1}} \\ \Omega_{\text{f2}} \\ \Omega_{\text{hub}} \\ \Omega_{\text{s1}} \\ \Omega_{\text{s2}} \\ (\Omega_{\text{f1}} - 0.55)^2 \\ (\Omega_{\text{f2}} - 0.55)^2 \\ (\Omega_{\text{hub}} - 0.55)^2 \\ (\Omega_{\text{s1}} - 0.55)^2 \\ (\Omega_{\text{s2}} - 0.55)^2 \end{bmatrix} = \begin{bmatrix} 0.55 \\ 0.55 \\ 0.55 \\ 0.55 \\ 0.55 \\ 0.025^2 \\ 0.025^2 \\ 0.025^2 \\ 0.025^2 \\ 0.025^2 \end{bmatrix} \quad (36)$$

For EPI in Fig 2C, we used a real NVP architecture with two coupling layers. Each coupling layer had two hidden layers of 10 units each, and we mapped onto a support of  $z \in \left[ \begin{bmatrix} 0 \\ 0 \end{bmatrix}, \begin{bmatrix} 10 \\ 8 \end{bmatrix} \right]$ . We have shown the EPI optimization that converged with maximum entropy across 2 random seeds and augmented Lagrangian coefficient initializations of  $c_0=0, 2$ , and 5.

721 **A.2.2 Primary visual cortex**722 The dynamics of each neural populations average rate  $x = \begin{bmatrix} x_E \\ x_P \\ x_S \\ x_V \end{bmatrix}$  are given by:

$$\tau \frac{dx}{dt} = -x + [Wx + h]_+^n \quad (37)$$

723 Some neuron-types largely lack synaptic projections to other neuron-types [53], and it is popular  
724 to only consider a subset of the effective connectivities [21].

$$W = \begin{bmatrix} W_{EE} & W_{EP} & W_{ES} & 0 \\ W_{PE} & W_{PP} & W_{PS} & 0 \\ W_{SE} & 0 & 0 & W_{SV} \\ W_{VE} & W_{VP} & W_{VS} & 0 \end{bmatrix} \quad (38)$$

725 By consolidating information from many experimental datasets, Billeh et al. [38] produce estimates  
726 of the synaptic strength (in mV)

$$M = \begin{bmatrix} 0.36 & 0.48 & 0.31 & 0.28 \\ 1.49 & 0.68 & 0.50 & 0.18 \\ 0.86 & 0.42 & 0.15 & 0.32 \\ 1.31 & 0.41 & 0.52 & 0.37 \end{bmatrix} \quad (39)$$

727 and connection probability

$$C = \begin{bmatrix} 0.16 & 0.411 & 0.424 & 0.087 \\ 0.395 & .451 & 0.857 & 0.02 \\ 0.182 & 0.03 & 0.082 & 0.625 \\ 0.105 & 0.22 & 0.77 & 0.028 \end{bmatrix} \quad (40)$$

728 Multiplying these connection probabilities and synaptic efficacies gives us an effective connectivity  
729 matrix:

$$W_{\text{full}} = C \odot M = \begin{bmatrix} 0.16 & 0.411 & 0.424 & 0.087 \\ 0.395 & .451 & 0.857 & 0.02 \\ 0.182 & 0.03 & 0.082 & 0.625 \\ 0.105 & 0.22 & 0.77 & 0.028 \end{bmatrix} \quad (41)$$

730 From use the entries of this full effective connectivity matrix that are not considered to be ineffectual.

732 We look at how this four-dimensional nonlinear dynamical model of V1 responds to different inputs,  
 733 and compare the predictions of the linear response to the approximate posteriors obtained through  
 734 EPI. The input to the system is the sum of a baseline input  $b = [1 \ 1 \ 1 \ 1]^\top$  and a differential  
 735 input  $dh$ :

$$h = b + dh \quad (42)$$

736 All simulations of this system had  $T = 100$  time points, a time step  $dt = 5\text{ms}$ , and time constant  
 737  $\tau = 20\text{ms}$ . And the system was initialized to a random draw  $x(0)_i \sim \mathcal{N}(1, 0.01)$ .

738 We can describe the dynamics of this system more generally by

$$\dot{x}_i = -x_i + f(u_i) \quad (43)$$

739 where the input to each neuron is

$$u_i = \sum_j W_{ij}x_j + h_i \quad (44)$$

740 Let  $F_{ij} = \gamma_i \delta(i, j)$ , where  $\gamma_i = f'(u_i)$ . Then, the linear response is

$$\frac{dx_{ss}}{dh} = F(W \frac{dx_{ss}}{dh} + I) \quad (45)$$

741 which is calculable by

$$\frac{dx_{ss}}{dh} = (F^{-1} - W)^{-1} \quad (46)$$

742 The emergent property we considered was the first and second moments of the change in rate  $dx$   
 743 between the baseline input  $h = b$  and  $h = b + dh$ . We use the following notation to indicate that  
 744 the emergent property statistics were set to the following values:

$$\mathcal{B}(\alpha, y) \leftrightarrow E \begin{bmatrix} dx_{\alpha,ss} \\ (dx_{\alpha,ss} - y)^2 \end{bmatrix} = \begin{bmatrix} y \\ 0.01^2 \end{bmatrix} \quad (47)$$

745 In the final analysis for this model, we sweep the input one neuron at a time away from the mode  
 746 of each inferred distributions  $dh^* = z^* = \text{argmax}_z \log q_\theta(z \mid \mathcal{B}(\alpha, 0.1))$ . The differential responses  
 747  $dx_{\alpha,ss}$  are examined at perturbed inputs  $h = b + dh^* + \Delta h_\alpha u_\alpha$  where  $u_\alpha$  is a unit vector in the  
 748 dimension of  $\alpha$  and  $\Delta h_\alpha \in [-15, 15]$ .

749 For each  $\mathcal{B}(\alpha, y)$  with  $\alpha \in \{E, P, S, V\}$  and  $y \in \{0.1, 0.5\}$ , we ran EPI with five different random  
 750 initial seeds using an architecture of four coupling layers, each with two hidden layers of 10 units.

751 We set  $c_0 = 10^5$ . The support of the learned distribution was restricted to  $z_i \in [-5, 5]$ .

<sup>752</sup> **A.2.3 Superior colliculus**

<sup>753</sup> There are four total units: two in each hemisphere corresponding to the Pro/Contra and Anti/Ipsi  
<sup>754</sup> populations. Each unit has an activity ( $x_i$ ) and internal variable ( $u_i$ ) related by

$$x_i(t) = \left( \frac{1}{2} \tanh \left( \frac{v_i(t) - \epsilon}{\zeta} \right) + \frac{1}{2} \right) \quad (48)$$

<sup>755</sup>  $\epsilon = 0.05$  and  $\zeta = 0.5$  control the position and shape of the nonlinearity, repsectively.

<sup>756</sup> We can order the elements of  $x_i$  and  $v_i$  into vectors  $x$  and  $v$  with elements

$$x = \begin{bmatrix} x_{LP} \\ x_{LA} \\ x_{RP} \\ x_{RA} \end{bmatrix} \quad v = \begin{bmatrix} v_{LP} \\ v_{LA} \\ v_{RP} \\ v_{RA} \end{bmatrix} \quad (49)$$

<sup>757</sup> The internal variables follow dynamics:

$$\tau \frac{dv}{dt} = -v + Wx + h + \sigma dB \quad (50)$$

<sup>758</sup> with time constant  $\tau = 0.09s$  and gaussian noise  $\sigma dB$  controlled by the magnitude of  $\sigma = 1.0$ . The  
<sup>759</sup> weight matrix has 8 parameters  $sW_P$ ,  $sW_A$ ,  $vW_{PA}$ ,  $vW_{AP}$ ,  $hW_P$ ,  $hW_A$ ,  $dW_{PA}$ , and  $dW_{AP}$  (Fig.  
<sup>760</sup> 4B).

$$W = \begin{bmatrix} sW_P & vW_{PA} & hW_P & dW_{PA} \\ vW_{AP} & sW_A & dW_{AP} & hW_A \\ hW_P & dW_{PA} & sW_P & vW_{PA} \\ dW_{AP} & hW_A & vW_{AP} & sW_A \end{bmatrix} \quad (51)$$

<sup>761</sup> The system receives five inputs throughout each trial, which has a total length of 1.8s.

$$h = h_{\text{rule}} + h_{\text{choice-period}} + h_{\text{light}} \quad (52)$$

<sup>762</sup> There are rule-based inputs depending on the condition,

$$h_{P,\text{rule}}(t) = \begin{cases} I_{P,\text{rule}} \begin{bmatrix} 1 & 0 & 0 & 1 \end{bmatrix}^\top, & \text{if } t \leq 1.2s \\ 0, & \text{otherwise} \end{cases} \quad (53)$$

<sup>763</sup>

$$h_{A,\text{rule}}(t) = \begin{cases} I_{A,\text{rule}} \begin{bmatrix} 0 & 1 & 1 & 0 \end{bmatrix}^\top, & \text{if } t \leq 1.2s \\ 0, & \text{otherwise} \end{cases} \quad (54)$$

<sup>764</sup> a choice-period input,

$$h_{\text{choice}}(t) = \begin{cases} I_{\text{choice}} \begin{bmatrix} 1 & 1 & 1 & 1 \end{bmatrix}^\top, & \text{if } t > 1.2s \\ 0, & \text{otherwise} \end{cases} \quad (55)$$

<sup>765</sup> and an input to the right or left-side depending on where the light stimulus is delivered.

$$h_{\text{light}}(t) = \begin{cases} I_{\text{light}} \begin{bmatrix} 1 & 1 & 0 & 0 \end{bmatrix}^\top, & \text{if } t > 1.2s \text{ and Left} \\ I_{\text{light}} \begin{bmatrix} 0 & 0 & 1 & 1 \end{bmatrix}^\top, & \text{if } t > 1.2s \text{ and Right} \\ 0, & t \leq 1.2s \end{cases} \quad (56)$$

<sup>766</sup> The input parameterization was fixed to  $I_{P,\text{rule}} = 10$ ,  $I_{A,\text{rule}} = 10$ ,  $I_{\text{choice}} = 2$ , and  $I_{\text{light}} = 1$

<sup>767</sup> To produce a Bernoulli rate of  $p_{LP}$  in the Left, Pro condition (we can generalize this to either cue,  
<sup>768</sup> or stimulus condition), let  $\hat{p}_i$  be the empirical average steady state (ss) response (final  $x_{LP}$  at end  
<sup>769</sup> of task) over M=500 gaussian noise draws for a given SC model parameterization  $z_i$ :

$$\hat{p}_i = E_{\sigma dB} [x_{LP,ss} | s = L, c = P, z_i] = \frac{1}{M} \sum_{j=1}^M x_{LP,ss}(s = L, c = P, z_i, \sigma dB_j) \quad (57)$$

<sup>770</sup> For the first constraint, the average over posterior samples (from  $q_\theta(z)$ ) to be  $p_{LP}$ :

$$E_{z_i \sim q_\phi} [E_{\sigma dB} [x_{LP,ss} | s = L, c = P, z_i]] = E_{z_i \sim q_\phi} [\hat{p}_i] = p_{LP} \quad (58)$$

<sup>771</sup> We can then ask that the variance of the steady state responses across gaussian draws, is the  
<sup>772</sup> Bernoulli variance for the empirical rate  $\hat{p}_i$ .

$$E_{z \sim q_\phi} [\sigma_{err}^2] = 0 \quad (59)$$

<sup>773</sup>

$$\sigma_{err}^2 = Var_{\sigma dB} [x_{LP,ss} | s = L, c = P, z_i] - \hat{p}_i(1 - \hat{p}_i) \quad (60)$$

<sup>774</sup> We have an additional constraint that the Pro neuron on the opposite hemisphere should have the  
<sup>775</sup> opposite value. We can enforce this with a final constraint:

$$E_{z \sim q_\phi} [d_P] = 1 \quad (61)$$

<sup>776</sup>

$$E_{\sigma dB} [(x_{LP,ss} - x_{RP,ss})^2 | s = L, c = P, z_i] \quad (62)$$

<sup>777</sup> We refer to networks obeying these constraints as Bernoulli, winner-take-all networks. Since the  
<sup>778</sup> maximum variance of a random variable bounded from 0 to 1 is the Bernoulli variance ( $\hat{p}(1 - \hat{p})$ ),

and the maximum squared difference between two variables bounded from 0 to 1 is 1, we do not need to control the second moment of these test statistics. In reality, these variables are dynamical system states and can only exponentially decay (or saturate) to 0 (or 1), so the Bernoulli variance error and squared difference constraints can only be undershot. This is important to be mindful of when evaluating the convergence criteria. Instead of using our usual hypothesis testing criteria for convergence to the emergent property, we set a slack variable threshold for these technically infeasible constraints to 0.05.

Training DSNs to learn distributions of dynamical system parameterizations that produce Bernoulli responses at a given rate (with small variance around that rate) was harder to do than expected. There is a pathology in this optimization setup, where the learned distribution of weights is bimodal attributing a fraction  $p$  of the samples to an expansive mode (which always sends  $x_{LP}$  to 1), and a fraction  $1 - p$  to a decaying mode (which always sends  $x_{LP}$  to 0). This pathology was avoided using an inequality constraint prohibiting parameter samples that resulted in low variance of responses across noise.

In total, the emergent property of rapid task switching accuracy at level  $p$  was defined as

$$\mathcal{B}(p) \leftrightarrow \begin{bmatrix} \hat{p}_P \\ \hat{p}_A \\ (\hat{p}_P - p)^2 \\ (\hat{p}_A - p)^2 \\ \sigma_{P,err}^2 \\ \sigma_{A,err}^2 \\ d_P \\ d_A \end{bmatrix} = \begin{bmatrix} p \\ p \\ 0.15^2 \\ 0.15^2 \\ 0 \\ 0 \\ 1 \\ 1 \end{bmatrix} \quad (63)$$

For each accuracy level  $p$ , we ran EPI for 10 different random seeds and selected the maximum entropy solution using an architecture of 10 planar flows with  $c_0 = 2$ . The support of  $z$  was  $\mathcal{R}^8$ .

#### 796 A.2.4 Rank-1 RNN

797 The network dynamics of neuron  $i$ 's rate  $x$  evolve according to:

$$\dot{x}_i(t) = -x_i(t) + \sum_{j=1}^N J_{ij}\phi(x_j(t)) + I_i \quad (64)$$

798 where the connectivity is comprised of a random and structured component:

$$J_{ij} = g\chi_{ij} + P_{ij} \quad (65)$$

799 The random bulk component has elements drawn from  $\chi_{ij} \sim \mathcal{N}(0, \frac{1}{N})$ , and the structured component  
800 is a sum of  $r$  unit rank terms:

$$P_{ij} = \sum_{k=1}^r \frac{m_i^{(k)} n_j^{(k)}}{N} \quad (66)$$

801 Rank-1 vectors  $m$  and  $n$  have elements drawn

$$m_i \sim \mathcal{N}(M_m, \Sigma_m)$$

802

$$n_i \sim \mathcal{N}(M_n, \Sigma_n)$$

803 The current has the following statistics:

$$I = M_I + \frac{\Sigma_{mI}}{\Sigma_m} x_1 + \frac{\Sigma_{nI}}{\Sigma_n} x_2 + \Sigma_\perp h$$

804 where  $x_1$ ,  $x_2$ , and  $h$  are standard normal random variables following the rank-1 input-driven example  
805 from [23].

806 We followed their prescription for deriving the consistency equations in the presence of chaos. The  
807  $\ddot{\Delta}$  equation is broken into the equation for  $\Delta_0$  and  $\Delta_\infty$  by the autocorrelation dynamics assertions.

$$\ddot{\Delta}(\tau) = -\frac{\partial V}{\partial \Delta}$$

808

$$\ddot{\Delta} = \Delta - \{g^2 \langle [\phi_i(t)\phi_i(t+\tau)] \rangle + \Sigma_m^2 \kappa^2 + 2\Sigma_{mI}\kappa + \Sigma_I^2\}$$

809 We can write out the potential function by integrating the negated RHS.

$$V(\Delta, \Delta_0) = \int \mathcal{D}\Delta \frac{\partial V(\Delta, \Delta_0)}{\partial \Delta}$$

810

$$V(\Delta, \Delta_0) = -\frac{\Delta^2}{2} + g^2 \langle [\Phi_i(t)\Phi_i(t+\tau)] \rangle + (\Sigma_m^2 \kappa^2 + 2\Sigma_{mI}\kappa + \Sigma_I^2)\Delta + C$$

811 We assume that as time goes to infinity, the potential relaxes to a steady state.

$$\frac{\partial V(\Delta_\infty, \Delta_0)}{\partial \Delta} = -\Delta + \{g^2 \langle [\phi_i(t)\phi_i(t+\infty)] \rangle + \Sigma_m^2 \kappa^2 + 2\Sigma_{mI}\kappa + \Sigma_I^2\} = 0$$

812

$$\Delta_\infty = g^2 \langle [\phi_i(t)\phi_i(t+\infty)] \rangle + \Sigma_m^2 \kappa^2 + 2\Sigma_{mI}\kappa + \Sigma_I^2$$

813 This can be written more explicitly in terms of the gaussian integrals which are relatively (with  
814 respect to nongaussian distributions) cheap to evaluate.

$$\Delta_\infty = g^2 \int \mathcal{D}z \left[ \int \mathcal{D}x \phi(\mu + \sqrt{\Delta_0 - \Delta_\infty}x + \sqrt{\Delta_\infty}z) \right]^2 + \Sigma_m^2 \kappa^2 + 2\Sigma_{mI}\kappa + \Sigma_I^2$$

815 Also, we assume that the energy of the system is preserved throughout the entirety of its evolution.

$$V(\Delta_0, \Delta_0) = V(\Delta_\infty, \Delta_0)$$

816

$$-\frac{\Delta_0^2}{2} + g^2 \langle [\Phi_i(t)\Phi_i(t)] \rangle + (\Sigma_m^2 \kappa^2 + 2\Sigma_{mI}\kappa + \Sigma_I^2) \Delta_0 + C = -\frac{\Delta_\infty^2}{2} + g^2 \langle [\Phi_i(t)\Phi_i(t)] \rangle + (\Sigma_m^2 \kappa^2 + 2\Sigma_{mI}\kappa + \Sigma_I^2) \Delta_\infty + C$$

817 We can arrange the terms into a difference of squares in  $\Delta_0$  and  $\Delta_\infty$ .

$$\frac{\Delta_0^2 - \Delta_\infty^2}{2} = g^2 ((\langle [\Phi_i(t)\Phi_i(t)] \rangle - \langle [\Phi_i(t)\Phi_i(t)] \rangle) + (\Sigma_m^2 \kappa^2 + 2\Sigma_{mI}\kappa + \Sigma_I^2)(\Delta_0 - \Delta_\infty))$$

818 Similarly, we write out the resulting equation explicitly in terms of the gaussian integrals present.

819

$$\begin{aligned} \frac{\Delta_0^2 - \Delta_\infty^2}{2} &= g^2 \left( \int \mathcal{D}z \Phi^2(\mu + \sqrt{\Delta_0}z) - \int \mathcal{D}z \int \mathcal{D}x \Phi(\mu + \sqrt{\Delta_0 - \Delta_\infty}x + \sqrt{\Delta_\infty}z) \right) \\ &\quad + (\Sigma_m^2 \kappa^2 + 2\Sigma_{mI}\kappa + \Sigma_I^2)(\Delta_0 - \Delta_\infty) \end{aligned}$$

820 This results in a set of consistency equations for the dynamic mean field variables  $\mu$ ,  $\kappa$ ,  $\Delta_0$ , and  
821  $\Delta_\infty$ . In order to obtain the values of these variables for a given parameterization, we must solve  
822 the following system of equations.

$$\begin{aligned} \mu &= F(\mu, \kappa, \Delta_0, \Delta_\infty) = M_m \kappa + M_I \\ \kappa &= G(\mu, \kappa, \Delta_0, \Delta_\infty) = M_n \langle [\phi_i] \rangle + \Sigma_{nI} \langle [\phi'_i] \rangle \\ \frac{\Delta_0^2 - \Delta_\infty^2}{2} &= H(\mu, \kappa, \Delta_0, \Delta_\infty) = g^2 \left( \int \mathcal{D}z \Phi^2(\mu + \sqrt{\Delta_0}z) - \int \mathcal{D}z \int \mathcal{D}x \Phi(\mu + \sqrt{\Delta_0 - \Delta_\infty}x + \sqrt{\Delta_\infty}z) \right) \\ &\quad + (\Sigma_m^2 \kappa^2 + 2\Sigma_{mI}\kappa + \Sigma_I^2)(\Delta_0 - \Delta_\infty) \\ \Delta_\infty &= L(\mu, \kappa, \Delta_0, \Delta_\infty) = g^2 \int \mathcal{D}z \left[ \int \mathcal{D}x \phi(\mu + \sqrt{\Delta_0 - \Delta_\infty}x + \sqrt{\Delta_\infty}z) \right]^2 + \Sigma_m^2 \kappa^2 + 2\Sigma_{mI}\kappa + \Sigma_I^2 \end{aligned} \tag{67}$$

823 We can solve these equations by simulating the following Langevin dynamical system.

$$\begin{aligned} x(t) &= \frac{\Delta_0(t)^2 - \Delta_\infty(t)^2}{2} \\ \Delta_0(t) &= \sqrt{2x(t) + \Delta_\infty(t)^2} \\ \dot{\mu}(t) &= -\mu(t) + F(\mu(t), \kappa(t), \Delta_0(t), \Delta_\infty(t)) \\ \dot{\kappa}(t) &= -\kappa + G(\mu(t), \kappa(t), \Delta_0(t), \Delta_\infty(t)) \\ \dot{x}(t) &= -x(t) + H(\mu(t), \kappa(t), \Delta_0(t), \Delta_\infty(t)) \\ \dot{\Delta_\infty}(t) &= -\Delta_\infty(t) + L(\mu(t), \kappa(t), \Delta_0(t), \Delta_\infty(t)) \end{aligned} \tag{68}$$

824 Then, the temporal variance, which is necessary for the gaussian posterior conditioning example, is  
825 simply calculated via

$$\Delta_T = \Delta_0 - \Delta_\infty \tag{69}$$

826 A.3 Supplementary Figures

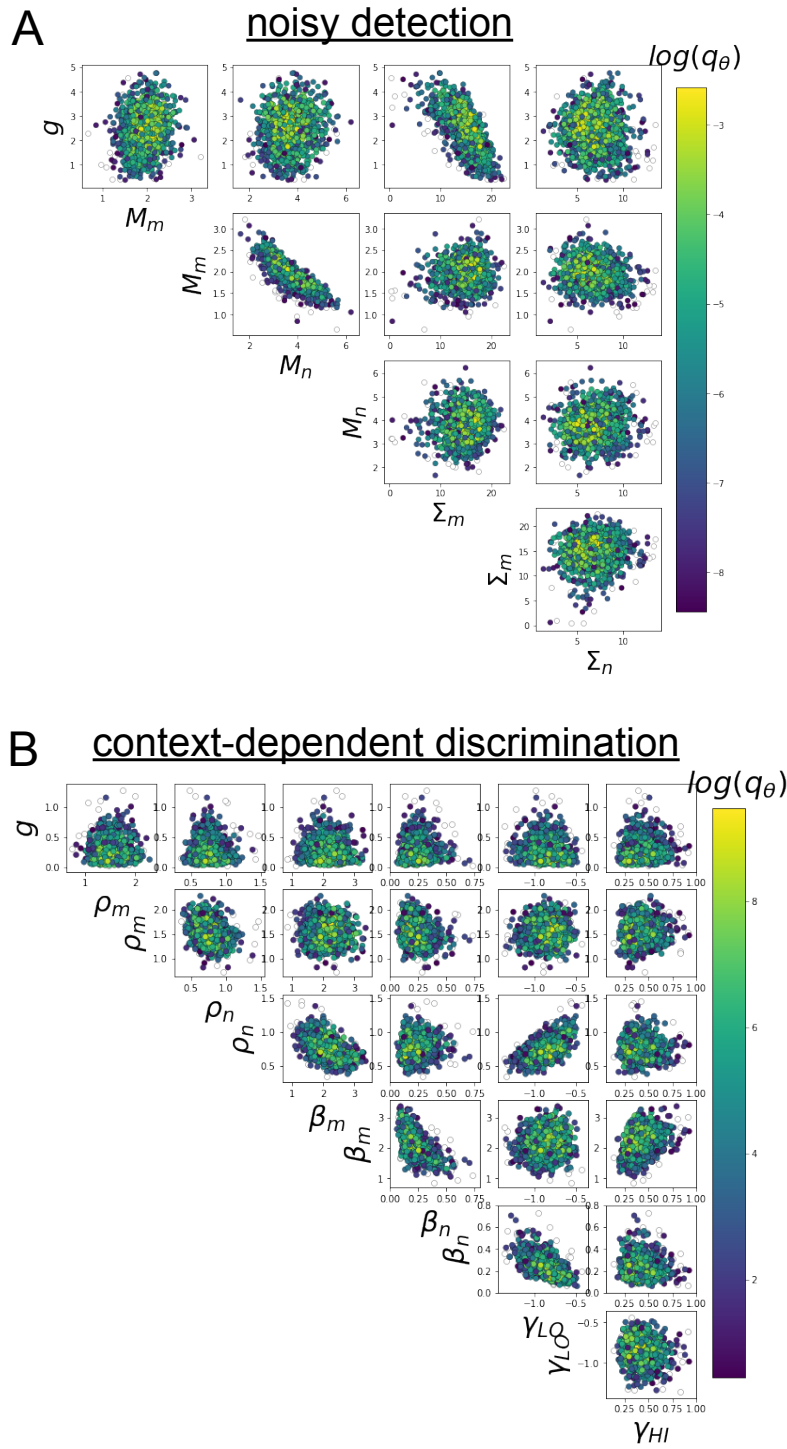


Fig. S1: A. EPI for rank-1 networks doing discrimination. B. EPI for rank-2 networks doing context-dependent discrimination.